Fitness landscape of the human immunodeficiency virus envelope protein that is targeted by antibodies

Raymond H. Y. Louie[a,b,1], Kevin J. Kaczorowski[c,d,1], John P. Barton[d,e,f], Arup K. Chakraborty[c,d,e,f,g,2], and Matthew R. McKay[a,h,2]

[a]Department of Electronic and Computer Engineering, Hong Kong University of Science and Technology, Kowloon, Hong Kong; [b]Institute for Advanced Study, Hong Kong University of Science and Technology, Kowloon, Hong Kong; [c]Department of Chemical Engineering, Massachusetts Institute of Technology, Cambridge, MA 02139; [d]Institute for Medical Engineering and Science, Massachusetts Institute of Technology, Cambridge, MA 02139; [e]Department of Physics, Massachusetts Institute of Technology, Cambridge, MA 02139; [f]Ragon Institute of Massachusetts General Hospital, Massachusetts Institute of Technology and Harvard, Cambridge, MA 02139; [g]Department of Chemistry, Massachusetts Institute of Technology, Cambridge, MA 02139; and [h]Department of Chemical and Biological Engineering, Hong Kong University of Science and Technology, Kowloon, Hong Kong

Contributed by Arup K. Chakraborty, December 11, 2017 (sent for review October 10, 2017; reviewed by Pamela J. Bjorkman and Martin Weigt)

HIV is a highly mutable virus, and over 30 years after its discovery, a vaccine or cure is still not available. The isolation of broadly neutralizing antibodies (bnAbs) from HIV-infected patients has led to renewed hope for a prophylactic vaccine capable of combating the scourge of HIV. A major challenge is the design of immunogens and vaccination protocols that can elicit bnAbs that target regions of the virus's spike proteins where the likelihood of mutational escape is low due to the high fitness cost of mutations. Related challenges include the choice of combinations of bnAbs for therapy. An accurate representation of viral fitness as a function of its protein sequences (a fitness landscape), with explicit accounting of the effects of coupling between mutations, could help address these challenges. We describe a computational approach that has allowed us to infer a fitness landscape for gp160, the HIV polyprotein that comprises the viral spike that is targeted by antibodies. We validate the inferred landscape through comparisons with experimental fitness measurements, and various other metrics. We show that an effective antibody that prevents immune escape must selectively bind to high escape cost residues that are surrounded by those where mutations incur a low fitness cost, motivating future applications of our landscape for immunogen design.

HIV | fitness landscape | envelope protein | statistical inference | broadly neutralizing antibodies

After over three decades of effort, there is now renewed hope for an effective vaccine against HIV. This is because of the isolation of broadly neutralizing antibodies (bnAbs) that are capable of neutralizing diverse HIV strains in vitro and progress made toward inducing them by vaccination (1–7), and reports of protection against infection for macaques immunized with a T cell-based vaccine (8, 9). However, much progress still needs to be made to realize the goal of deploying an effective vaccine, and also to develop rational strategies for optimizing immunogens and vaccination protocols. A related issue is the choice of combinations of bnAbs for passive therapy of infected persons, an approach that has shown promise in humans and macaques (10–12).

Because HIV is highly mutable, one key challenge is that the virus can evolve mutations that abrogate the binding of antibodies to HIV's envelope proteins or T cell receptors to peptides derived from viral proteins, while also preserving fitness (the ability to properly assemble the virus, replicate, and propagate infection). This allows HIV to escape from human immune responses. On the other hand, some parts of the viral proteome are vulnerable to mutations because they result in a severe loss of fitness. Vaccination strategies aimed at targeting these parts of the proteome and not the ones that readily allow escape might be effective. The design of effective vaccination strategies would therefore benefit from knowledge of the fitness landscape of viral proteins—that is, knowledge of the fitness of the virus as a function of its amino acid sequence.

A conventional approach to estimate the fitness landscape of a virus is to assume that the fitness of a sequence is directly related to the extent to which the amino acids at a residue are conserved in circulating viral strains; more conserved residues are ones where mutations are predicted to result in a larger fitness penalty. This approach was used to obtain a landscape experimentally for the HIV envelope protein, gp160 (13), and computationally for other HIV proteins (14, 15). However, it ignores epistatic coupling between mutations at different residues, which is known to be an important factor for viral fitness (16–18). For example, if a mutation that allows the virus to evade an immune response occurs at a particular relatively conserved residue, it is likely to significantly impair viral fitness. However, if another mutation at a different residue has a compensatory effect, the fitness cost incurred by making the primary immune-evading mutation can be partially restored. Because HIV is highly mutable and also exhibits a high replication rate, such compensatory mutations can be accessed in vivo, and have been found to be a significant factor in determining viral fitness and mutational escape pathways (16–19). Thus, to define the mutational vulnerabilities of a virus like HIV in vivo, and thus guide the design of vaccination strategies, the desired fitness landscape must include the effects

Significance

An effective vaccine for HIV is still not available, although recent hope has emerged through the discovery of antibodies capable of neutralizing diverse HIV strains. Nonetheless, there exist mutational pathways through which HIV can evade known broadly neutralizing antibody responses. An ideal vaccine would elicit broadly neutralizing antibodies that target parts of the virus's spike proteins where mutations severely compromise the virus's fitness. Here, we employ a computational approach that allows estimation of the fitness landscape (fitness as a function of sequence) of the polyprotein that comprises HIV's spike. We validate the inferred landscape through comparisons with diverse experimental measurements. The availability of this fitness landscape will aid the rational design of immunogens for effective vaccines.

Author contributions: R.H.Y.L., K.J.K., A.K.C., and M.R.M. designed research; R.H.Y.L., K.J.K., A.K.C., and M.R.M. performed research; R.H.Y.L., K.J.K., J.P.B., A.K.C., and M.R.M. analyzed data; and R.H.Y.L., K.J.K., J.P.B., A.K.C., and M.R.M. wrote the paper.

Reviewers: P.J.B., California Institute of Technology; and M.W., Université Pierre et Marie Curie.

The authors declare no conflict of interest.

[1]R.H.Y.L. and K.J.K. contributed equally to this work.

[2]To whom correspondence may be addressed. Email: arupc@mit.edu or m.mckay@ust.hk.

This article contains supporting information online at www.pnas.org/lookup/suppl/doi:10.1073/pnas.1717765115/-/DCSupplemental.

of coupling between mutations at different residues. Unfortunately, despite continuing progress (13, 20, 21), experimentally obtaining a fitness landscape that includes coupling information for the majority of proteins in HIV is infeasible, because the number of experimental fitness values that need to be measured is prohibitively large. For example, there are on the order of 10^7 experimental fitness values that would need to be measured for gp160 (Fig. 1), the polyprotein that comprises the HIV spike that is targeted by antibodies.

One approach that has been successful in obtaining the fitness landscape of HIV proteins, including the effects of couplings, has relied on inferring this information from the sequences of circulating strains [a multiple sequence alignment (MSA)] (19, 22–25). First, a maximum-entropy–based computational approach (*SI Appendix*, *Text 2.1*) was used to infer a "prevalence landscape" from the sequence data, taking into account couplings between residues; the prevalence landscape describes the probability of observing a virus with particular protein sequence in circulation (Fig. 2*A*). Theoretical analyses and tests against in vitro and clinical data (19, 22, 26) suggest that, because of the evolutionary history of HIV and the diversity of (largely ineffective) immune responses that the HIV population has been subjected to, the prevalence landscape is a reasonably good proxy for the fitness landscape. This approach has been applied and validated for various internal proteins of HIV (19, 22–25). Similar methods have also been employed to predict the fitness effects of mutations in bacterial proteins (27). However, a fitness landscape for gp160 has not been previously obtained, despite its importance as a target of antibody responses. This is because the inference problem is far more challenging. In particular, the gp160 primary sequence is more than twice as long as any other HIV protein, and it is also among the most variable. This leads to an explosion in the number of model parameters to be estimated (Fig. 1). Standard inference approaches, such as those based on gradient descent algorithms [commonly referred to as Boltzmann machine-learning (BML) methods] or Markov chain Monte Carlo-based simulation methods (22, 28) are intractable for the gp160 protein.

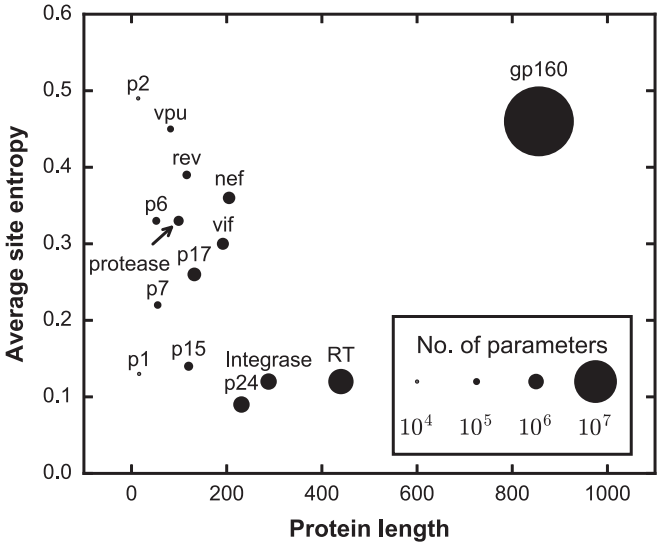

Fig. 1. For different HIV proteins, the number of parameters, average site entropy, and protein length are shown. gp160 has orders of magnitude more parameters than the majority of the other HIV proteins, the longest length, and one of the largest average site entropy. Note that, to obtain a landscape purely based on experiments, the number of required in vitro experimental fitness values is proportional to the number of parameters. The amino acid MSA for each protein was downloaded from the Los Alamos National Laboratory (LANL) HIV sequence database (https://www.hiv.lanl.gov/).

To address this issue, we introduce a computational framework (Fig. 2*B*) that efficiently and accurately calculates the parameters of a maximum-entropy model for the gp160 fitness landscape. We validate the inferred fitness landscape by testing predictions of fitness against in vitro measurements of the fitness of nearly 100 HIV strains bearing mutations in gp160, testing predictions of protein contacts against structural data, and showing that our fitness landscape is consistent with known escape mutations. The fitness landscape that we report can help guide the design of immunogens aimed toward eliciting bnAbs, the choice of bnAb combinations for passive therapy, and the choice of immunogens for the T cell component of a vaccine.

Computational Method

The fitness landscape is specified as a probabilistic model, chosen as the model having the maximum entropy (i.e., the model least biased by intuition), subject to the constraint of reproducing the single- and double-mutant probabilities observed in the MSA (*SI Appendix*, Eq. **S5**). For a given length-L amino acid sequence $\mathbf{x}=[x_1,x_2,\ldots,x_L]$, where x_i can take on any of the 20 naturally occurring amino acids or gap in the MSA, this maximum-entropy model assigns the probability (22):

$$p_{\mathbf{h},\mathbf{J}}(\mathbf{x})=\frac{\exp[-E(\mathbf{x})]}{\sum_{\mathbf{x}'}\exp[-E(\mathbf{x}')]},\ E(\mathbf{x})=\sum_{i=1}^{L}h_i(x_i)+\sum_{i=1}^{L}\sum_{j=i+1}^{L}J_{ij}(x_i,x_j), \quad [1]$$

where, in analogy with statistical mechanics, we refer to $E(\mathbf{x})$ as the energy of sequence $\mathbf{x}$. The parameters $h_i(x_i)$ and $J_{ij}(x_i,x_j)$, referred to as fields and couplings, respectively, can be obtained by solving the following convex optimization problem (*SI Appendix*, *Text 2.1*):

$$(\mathbf{h}^*,\mathbf{J}^*)=\arg\min_{\mathbf{h},\mathbf{J}}\mathrm{KL}\left(p_0\|\,p_{\mathbf{h},\mathbf{J}}\right), \quad [2]$$

subject to the single- and double-mutant probabilities matching those in the MSA (*SI Appendix*, Eq. **S5**). Here, p_0 denotes the patient-weighted sequence probability distribution from the MSA (*SI Appendix*, *Text 2.1*), and $\mathrm{KL}(p_0\|\,p_{\mathbf{h},\mathbf{J}})$ denotes the Kullback–Leibler divergence between p_0 and $p_{\mathbf{h},\mathbf{J}}$ (*SI Appendix*, Eq. **S7**). This problem can be solved in principle by BML algorithms; however, such algorithms require computing a gradient function that involves an exponential number of terms in L, thereby making direct computation infeasible for the gp160 protein. A solution to this challenge is provided for other HIV proteins by use of a cluster expansion approach along with BML (24, 29, 30). However, achieving reliable statistical inference for gp160 is difficult due to the large parameter space (Fig. 1) and the relatively small number of sequences available for gp160 (*SI Appendix*, *Text 1*). The method described here addresses these issues via three main steps (Fig. 2*B* and *SI Appendix*, *Text 2*). The most important of these is the introduction of a computationally efficient algorithm that produces accurate initial estimates of the fields and couplings. This method is augmented by the refinement of these estimates using BML, which, due to the accuracy of the initialization, converges quickly, and the application of a variable-combining method for reducing the effective number of parameters, which is more systematic than past such approaches.

Our approach for providing an initial estimate of the field and coupling parameters is based on the principle of minimum probability flow (MPF) (31), which was successfully applied to different applications such as deep belief networks and independent component analysis (31), although to our knowledge it has yet to be used for the analysis of protein sequence data. We first describe the general idea of MPF as applied to our maximum-entropy problem, and then discuss some distinctions with related work. The MPF principle leads to replacing $p_{\mathbf{h},\mathbf{J}}$ in

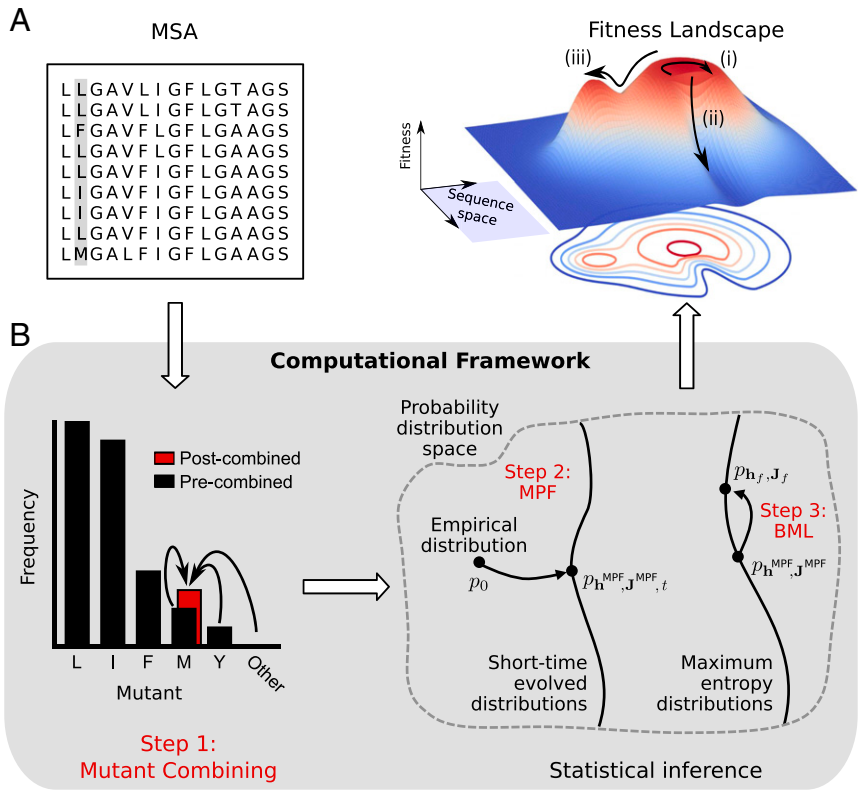

Fig. 2. (*A*) The general framework used for inferring a fitness landscape for gp160. Protein sequence data, in the form of a multiple sequence alignment (MSA), is used to infer a maximum-entropy, or least-biased, probability distribution of sequences, subject to recapitulating the observed one- and two-point mutation probabilities. This distribution is termed the sequence prevalence landscape (*SI Appendix, Text 2.1*). Based on past work on other HIV proteins, we assume that protein fitness is directly proportional to sequence prevalence. As shown in a schematic depiction (*Right*), the fitness landscape traces out fitness values over the space of possible protein sequences and highlights several features expected of the gp160 landscape: HIV often escapes even in the presence of bnAbs, suggesting that many mutational pathways may have small fitness costs (*i*); other escape pathways may lead to a large decrease in fitness (*ii*); but compensatory mutations can restore fitness (*iii*). (*B*) Our computational framework includes three steps to solve the maximum-entropy problem. Step 1 involves reducing the number of mutants from the original MSA (*SI Appendix, Text 2.3*). The bar chart shows the single-mutant probabilities for one particular residue (highlighted in gray in the MSA depicted in *A*). Infrequent amino acids are combined together and treated as a single mutant ("post-combined"). Step 2 involves solving a modified minimum probability flow (MPF) objective function involving the KL divergence between the empirical distribution and a short-time evolved distribution (Eq. **3**), to include regularization and arbitrary number of mutants (*SI Appendix, Text 2.3*). Step 3 involves refining the parameters from step 2 using a Boltzmann machine-learning (BML) algorithm (*SI Appendix, Text 2.3*), which produces the field ($\mathbf{h}_f$) and coupling ($\mathbf{J}_f$) parameters of the landscape.

the optimization problem (Eq. **2**) with an alternate (related) distribution that is simpler to optimize, and which is expected to yield an accurate approximation to the desired maximum-entropy solution. Specifically, the maximum-entropy form (Eq. **1**) is viewed as the equilibrium distribution of a Markov process with appropriately specified deterministic dynamics (*SI Appendix, Text 2.3*) that evolves the empirical data distribution p_0 toward $p_{\mathbf{h},\mathbf{J}}$. Based on these dynamics, the original optimization problem (Eq. **2**) is replaced with the alternative problem:

$$\left(\mathbf{h}^{\mathrm{MPF}},\mathbf{J}^{\mathrm{MPF}}\right)=\arg\min_{\mathbf{h},\mathbf{J}}\mathrm{KL}\left(p_0\|\,p_{\mathbf{h},\mathbf{J};t}\right), \qquad [3]$$

where $p_{\mathbf{h},\mathbf{J};t}$ (*SI Appendix*, Eq. **S13**) represents the distribution obtained by running the dynamics for time t. While this distribution, as well as the associated KL divergence in Eq. **3**, is still quite complicated, it is greatly simplified for small values of t. Specifically, for small t, the KL divergence is well approximated by a linear function of t (*SI Appendix, Text 2.3*):

$$\mathrm{KL}\left(p_0\|\,p_{\mathbf{h},\mathbf{J};t}\right)\approx t\mathrm{K}_{\mathbf{h},\mathbf{J}},$$

where $\mathrm{K}_{\mathbf{h},\mathbf{J}}$ is a simple function of the field and coupling parameters $\mathbf{h}$, $\mathbf{J}$ (see *SI Appendix*, Eq. **S16** for the explicit formula). The parameters that minimize this function can then be easily found using a standard gradient descent algorithm. Importantly, choosing small t to facilitate an expansion of the KL divergence (Eq. **3**) results in an efficient objective function $\mathrm{K}_{\mathbf{h},\mathbf{J}}$, which involves only a quadratic number of terms in L (*SI Appendix*, Eq. **S15**), as opposed to the original problem (Eq. **2**), which was exponential in L. The estimates obtained by minimizing $\mathrm{K}_{\mathbf{h},\mathbf{J}}$ are also statistically consistent (31): if the data are drawn from the maximum-entropy model (Eq. **1**), then the parameter estimates become arbitrarily accurate given a sufficiently large number of samples.

Of direct relevance to our problem, the MPF procedure was previously applied to learn Ising spin-glass models (31), which have the form of the maximum-entropy distribution (Eq. **1**), but restricted to modeling only two amino acids per residue. Our approach (*SI Appendix, Text 2.3*) extends that procedure to make it suitable for the gp160 problem. First, we allow for arbitrary numbers of amino acids per residue, which is essential due to the large sitewise amino acid variability observed in the MSA. Second, we introduce regularization to control sampling noise (*SI Appendix*, Eq. **S17** and *Text 2.3*), which is required due to the large number of parameters and limited sequence data for gp160. The regularization parameters are chosen such that the model parameters yield a suitable balance between statistical overfitting and underfitting, based on a previously defined metric

(32). This is achieved by appropriately biasing the estimated single- and double-mutant probabilities through regularization, to faithfully capture real mutational variability and ignore variability resulting from finite sampling (*SI Appendix*, Eq. **S18** and *Text 2.4*).

By solving a proxy optimization problem, the MPF inference procedure yields a set of inferred model parameters that serve as approximations to the desired optimal maximum-entropy parameters (Eq. **2**). These parameters are then refined using a gradient descent-based BML algorithm, referred to as RPROP (33), with an additional regularization term (*SI Appendix*, *Text 2.4*). While BML algorithms are intractable when applied to the gp160 maximum-entropy problem with arbitrary initialization (Eq. **2**), such algorithms can converge quickly when accurate initial parameters resulting from the MPF-based inference procedure are provided.

Multiple amino acids are observed at each residue of gp160 in the MSA. Here, we restrict the number of amino acids explicitly modeled in the inference procedure to decrease the computational burden (30). We propose a general data-driven approach to combine the least frequent mutants (nonconsensus amino acids) together. Combining such mutants also makes sense statistically since the low-frequency mutants are particularly sensitive to sampling noise, and their corresponding parameters are more challenging to meaningfully estimate. This approach, applicable to any protein, can substantially decrease the number of parameters to be estimated. To achieve this, as in the past (30), for residue i we model only the k_i most frequent mutants, while grouping the remaining $q_i - k_i + 1$ mutants together, where q_i denotes the number of mutants at residue i as observed in the MSA. Here, k_i is chosen such that, upon grouping, the entropy at residue i is at least a certain fraction ϕ of the corresponding entropy without grouping. The design question is to choose an appropriate value of ϕ. In previous work (19, 22, 30), this factor was chosen arbitrarily. However, for a protein like gp160, which has a significantly larger number of parameters than the other HIV proteins (Fig. 1), a more judicious choice of ϕ may have considerable benefits. A lower value will combine more mutants together, thus decreasing the number of parameters to be estimated and reducing the computational burden. However, combining too many mutants can result in a loss of useful information regarding amino acid identities. These quantities can be quantified in the form of a statistical bias (*SI Appendix*, *Text 2.2*).

To balance these competing issues systematically, we introduce a method for selecting ϕ based on the sequence data (*SI Appendix*, *Text 2.2*). It is described briefly as follows. For any given ϕ, for each residue i we can specify k_i as indicated above. Letting $f_i(a)$ denote the frequency of amino acid a at residue i, this leads to a modified (sparsified) model in which the frequencies of the modified model are now as follows:

$$\bar{f}_i(a) = \begin{cases} f_i(a) & \text{if } a < k_i + 1 \\ \bar{f}_i & \text{if } a = k_i + 1 \\ 0 & \text{if } a > k_i + 1 \end{cases}, \qquad [4]$$

where $\bar{f}_i = \sum_{a=k_i+1}^{q_i} f_i(a)$ represents the frequency of the coarse-grained amino acid. The squared error/bias of this model (i.e., for the specific ϕ) at residue i is then estimated as $\sum_{a=1}^{q_i} [f_i(a) - \bar{f}_i(a)]^2$, while the total variance of the amino acid frequencies at residue i is estimated as $\sum_{a=1}^{q_i} f_i(a)[1 - f_i(a)]/P$. Our aim is to select a level of coarse-graining that corresponds to the fractional entropy captured, ϕ, such that these quantities are commensurate. Intuitively, this approach seeks to select the sparsest model (i.e., choosing ϕ giving the most coarse-grained combining) such that the resulting errors caused by combining do not generally exceed the statistical fluctuations in the estimated amino acid frequencies from the MSA. A significant advantage of such variable selection approach is that it can substantially reduce the number of maximum-entropy parameters to infer (i.e., reducing the number of fields and couplings in Eq. **1**), thereby simplifying the parameter estimation problem, but without sacrificing the predictive power of the inferred model.

To this end, denoting the ratio of fractional error to variance in the amino acid frequencies in the data (see above) as $\beta_i(\phi)$ and letting $\langle \beta_i(\phi) \rangle$ be the average of $\beta_i(\phi)$ taken over all residues i, we select ϕ by numerically searching for a value that yields $\langle \beta_i(\phi) \rangle$ close to 1.

Results

We applied the computational framework to a MSA of HIV-1 clade B gp160 amino acid sequences downloaded from the Los Alamos National Laboratory (LANL) HIV sequence database (https://www.hiv.lanl.gov/). The MSA was processed to ensure both sequence and residue quality (*SI Appendix*, *Text 2.1*), resulting in $L = 815$ residues and 20,043 sequences belonging to 1,918 patients. These sequences were highly variable, involving an average pairwise Hamming distance of 0.1824, normalized by L.

The Computational Method Is Fast and Accurately Captures the Observed Sequence Statistics. When applied to the MSA of gp160, our computational framework took only 2.5 d of CPU time (12 h for MPF, 2 d for convergence of the subsequent BML) on a 16-core node with 128-GB RAM and 2.7-GHz processing speed. This is significant given the large number of parameters that needed to be estimated (~4.4 million). The computational efficiency was aided by the initial variable selection phase, which reduced the number of parameters by a factor of 6. The inferred model accurately reproduced the single- and double-mutant probabilities observed in the MSA (Fig. 3 *A* and *B*), as required. The fast convergence of the BML algorithm in our framework was due both to the significant reduction in parameters achieved with the initial selection phase, as well as the high accuracy of the initialization parameters estimated by MPF (Fig. 3 *A* and *B*). Nonetheless, the BML refinement led to a better fit of the single- and double-mutant probabilities, while also yielding a clear improvement in terms of connected correlations (Fig. 3*C*). Finally, while the model was designed to explicitly reproduce single- and double-mutant probabilities, the inferred parameters also captured higher order statistics (Fig. 3*D*). This information was not reflected by the model produced by MPF, emphasizing the importance of the subsequent BML estimation phase.

Inferred Fitness Landscape Accurately Predicts in Vitro Replicative Fitness Measurements. To assess the ability of the inferred model to capture the fitness of different strains of gp160, we compared predictions based on this model to in vitro measurements of HIV fitness. We compiled 98 fitness measurements from in vitro experiments using competition (16, 17, 34, 35) or infectivity assays (18, 36). Strains used in these experiments were constructed by engineering single, double, or higher order mutations on a CCR5-tropic strain. However, there was no explicit consideration given to choosing higher order mutants that exhibit epistatic coupling, known to be important in vivo (*Discussion*). The metric of fitness in our model is the energy, E in Eq. **1**. Larger values of E correspond to less-fit strains. Based on the values of E computed using our fitness landscape, we predicted the relative fitness of the experimentally tested strains. We then determined the rank correlation [based on a weighted Spearman correlation measure (*SI Appendix*, Eq. **S19** and *Text 3*)] between these values of E and the measured fitness values (Fig. 4*A*). As anticipated, we found a strong weighted negative correlation (*SI Appendix*, Eq. **S19**), given by $\bar{\rho} = -0.74$ between model energies and viral fitness (see *SI Appendix*, Fig. S1 and *Text 3* for results for each individual experiment). These results demonstrate the ability of the inferred landscape to discriminate the relative intrinsic fitness of different HIV strains with mutations in gp160.

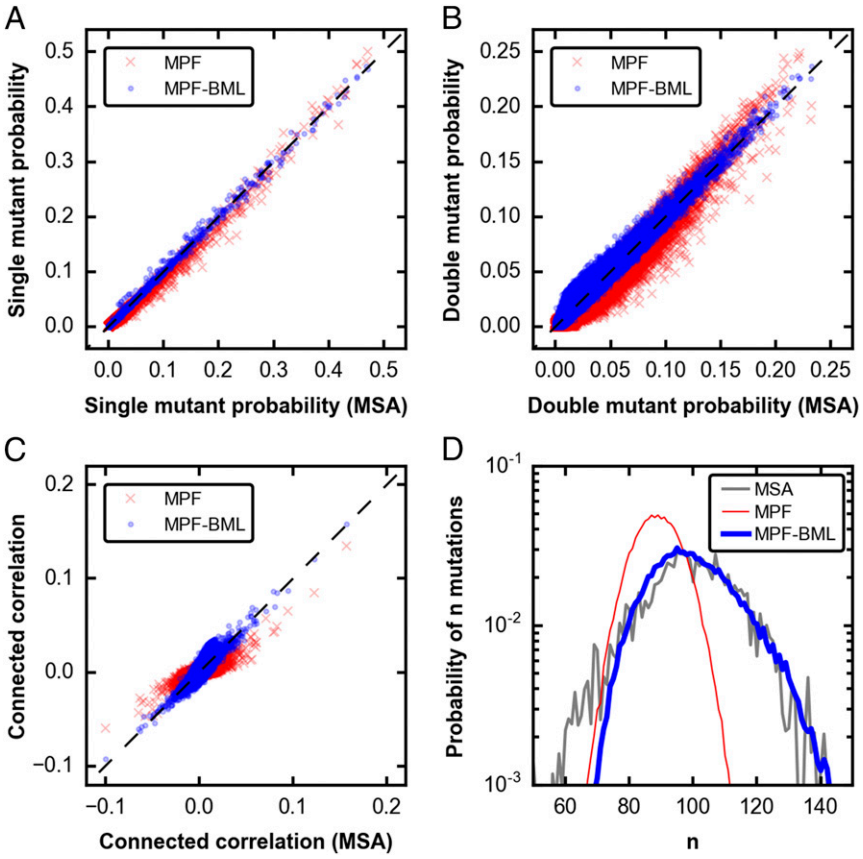

Fig. 3. (*A* and *B*) Scatter plot of the MPF/MPF-BML vs. MSA single (double)-mutant probabilities, verifying that the inferred fields and couplings for both MPF and final model with additional BML refinement, labeled MPF-BML, can accurately reproduce the single (double)-mutant probabilities. (*C*) Scatter plot of the connected correlations (covariances), demonstrating the benefits of BML refinement over MPF alone. (*D*) Probability of number of mutations, verifying that the inferred fields and couplings after BML, but not after MPF alone, accurately reproduce higher order statistics beyond the single- and double-mutant probabilities (which were not inputs to the inference procedure).

We note that the predicted combining factor $\phi = 0.95$, established at the initial variable combining phase, produced a landscape that achieved the strongest correlation with fitness values compared with other values of ϕ (*SI Appendix*, Table S3).

Inferred Couplings Predict Contact Residues. We expect that strongly interacting pairs of residues should be associated with strong couplings. For example, we previously showed in other HIV proteins that strong couplings are associated with compensatory mutations or those that interact synergistically to make the double mutant especially unfit (22, 24, 25). We used the couplings inferred for gp160 to predict residues that are likely to be in contact in the protein's native state, which can be determined from crystal structures. The rationale is that residues that are in close spatial proximity in the protein's native state should have a greater influence on each other, and this effect can be quantified by a measure dependent on the corresponding couplings (37, 38). Similar approaches were originally developed to predict residues in contact in the 3D protein structure on the basis of their inferred interactions, and have recently been extended to identify sets of interacting proteins on the basis of strong inferred couplings (39, 40). As our model is inferred from in vivo data, we anticipate that the model should capture contacts in the gp160 trimer that constitutes the functionally important HIV spike, not just contacts between residues in monomers of gp120 or gp41. To test this, we compared the top predicted contacts (a function of our model couplings) with known contacts based on a crystal structure of SOSIP (41), a synthetic mimic of the native gp160 trimer [Protein Data Bank (PDB) ID code 5D9Q]. The results (Fig. 4*B*) demonstrate that the couplings in our inferred model are predictive of protein contacts for the gp160 trimeric spike of HIV. We found similar results for nine other crystal structures (*SI Appendix*, Fig. S3).

Although our inferred couplings can predict contacts well, apparent false positives are still observed. To examine this further, we considered the top 20 residue pairs that have the largest average product correction–direct information (APC-DI) scores, in which 8 of these are not predicted to be in contact (*SI Appendix*, Table S4). With the exception of one residue pair, these residues are located in the V2 or V4 loop, or are CD4 contacts. For the residues in the V2 loop or those that are CD4 contacts, a possible reason for these residue pairs having a high APC-DI score is due to the conformational changes that occur when gp160 interacts with CD4 and other coreceptors, which is not captured in the protein structures. Indeed, conformational changes due to gp160–CD4 interaction have been well documented for the V2 loop (42). These conformational changes may favor or disfavor certain pairs of mutations. For the 389–417 residue pair in the V4 loop, it is not clear why this pair has a high APC-DI score, although we note that these residues are located near the base of the loop.

Observed Mutations in Footprints of CD4 Binding Site bnAbs Have Low Fitness Costs. As further validation of our landscape, we investigated whether its predictions explain why certain mutations that change the binding of bnAbs are observed in circulating virus strains, and others are not. Based on crystal structures, we first determined the residues on gp160 that were in contact with a number of CD4 binding-site bnAbs (listed in *SI Appendix*, *Text 8*). The CATNAP online tool (43) is a database of experimental IC-50 measurements between panels of bnAb–virus pairs. To determine whether mutations in gp160 residues that were in contact with the bnAbs affected binding, we used a feature in CATNAP that uses Fisher's exact test to identify viral amino acids that are statistically associated ($P < 0.05$) with either high or low IC-50 scores. This analysis allowed us to determine a set

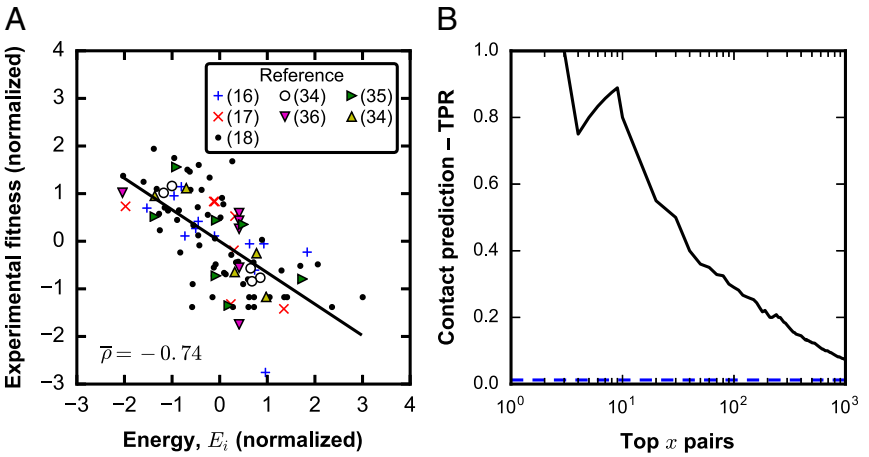

Fig. 4. (*A*) Normalized logarithm of fitness vs. normalized energy for all seven experimental datasets collected from the literature for a combining factor of $\phi = 0.95$. References for the datasets are shown in the legend. Normalization is performed by subtracting the mean of each dataset and dividing by the SD. A strong weighted correlation (*SI Appendix*, Eq. **S25**) is observed (see also *SI Appendix*, Fig. S1 for individual experiments). (*B*) Fraction of contacts in the top *x* predicted pairs which are actually in contact [true-positive rate (TPR)] vs. the top *x* predicted pairs as determined by a high value of the coupling constant (black line). True contacts are calculated from a crystal structure of the SOSIP trimer (5D9Q). These data show that the pairs with high predicted values of the coupling constants predict true contacts observed in the crustal structure of the SOSIP trimer. Also graphed is the total number of contacts (observed in the crystal structure) divided by the total number of pairs (horizontal blue line), which represents the probability of choosing a pair in contact purely by chance. Only pairs that are more than five residues apart in sequence space are considered, and out of these pairs, two residues are assumed to be in contact if they are <8 Å apart. PDB ID code 5D9Q.

of residues in gp160 contained in the footprints of CD4 binding-site antibodies that are statistically associated with a change in IC-50 for at least one mutant amino acid. These residues have at least one amino acid substitution pathway that changes the binding affinity to bnAbs. We analyzed only viral strains observed in the MSA that correspond to viable viruses.

At the identified set of residues, we further classify specific amino acid mutations as either "observed," defined as those mutations associated with a change in binding to bnAbs in the CATNAP data and observed in the MSA, or "unobserved," defined as mutations that are not in the CATNAP data (irrespective of whether they are observed in the MSA). We found that roughly 90% of these unobserved mutations are absent from the MSA (*SI Appendix*, Fig. S5*A*), and therefore are likely to be unviable. Furthermore, the largest frequency for an amino acid mutation present in the MSA but absent from CATNAP is small [i.e., less than 5% (*SI Appendix*, Fig. S5*B*)], while the amino acid mutations observed in the CATNAP data are representative of those observed in the MSA (*SI Appendix*, Fig. S5*C*). We expect, therefore, that observed mutations would be associated with lower fitness costs than unobserved mutations, since they are associated with viable viruses, and hence they are expected to escape the immune pressure with the least effect on the ability to propagate infection.

To assess whether the predictions of our fitness landscape are consistent with these expectations, we employed a measure that has been used before to predict the fitness cost of a mutation averaged over all sequence backgrounds (24). Specifically, we compute the change in energy associated with the mutation averaged over a Monte Carlo sample of diverse sequence backgrounds obtained using our fitness landscape to approximate:

$$\Delta E_{i,\mathbf{h}_f,\mathbf{J}_f}(a) = \sum_{\mathbf{x},x_i=0} \left[E_{\mathbf{h}_f,\mathbf{J}_f}(\mathbf{x}') - E_{\mathbf{h}_f,\mathbf{J}_f}(\mathbf{x})\right] p_{\mathbf{h}_f,\mathbf{J}_f}(\mathbf{x}), \qquad [5]$$

where $\mathbf{h}_f$ and $\mathbf{J}_f$ represent the final parameters after BML refinement, and the summation is over all sequences $\mathbf{x}$ having the consensus amino acid ("0") at the ith residue. Here, $\mathbf{x}'$ is identical to $\mathbf{x}$, except with the amino acid at residue i replaced by a. This measure quantifies the typical change in fitness upon introducing this mutation at the residue across various sequence backgrounds in circulating viruses. A positive fitness cost implies a decrease in fitness (22, 24). As predicted, the observed mutations at the residues that affect IC-50 are predicted to incur a lower average fitness cost compared with amino acid mutations that were not observed (Fig. 5*A*).

The difference in mean fitness cost between observed and unobserved mutations is due to the presence of some observed mutations with very low fitness costs, coupled with high fitness costs for many unobserved mutations. The existence of the low-fitness cost pathways that also likely abrogate binding implies that even canonically broad and potent bnAbs are imperfect. In patients who develop bnAbs upon natural infection, the viral quasispecies readily evolves escape mutations (1); escape mutations also eventually arise when bnAbs are administered passively (44), even when multiple bnAbs are used in concert (44, 45).

To further test our fitness landscape, we next focused on the gp160 residues in CD4 binding site antibody footprints that are not statistically associated with changes in IC-50 according to the analysis using CATNAP. We first examined whether the amino acid mutations at these residues that are observed are biochemically similar to each other and to the consensus amino acid at the residue. To determine this, for each residue, we calculated the biochemical similarity between the nonconsensus amino acid and the respective consensus amino acid, averaged over all sequences in the panels with nonconsensus amino acid at that residue (*SI Appendix*, Eq. **S25**). The similarity matrix (46) assigns to each pair of amino acids a similarity score ranging from 0 to 6, with matching amino acids assigned a value of either 5 or 6, where 6 is assigned to the more rare, unique amino acids (F, M, Y, H, C, W, R, and G) to reflect this. Mismatched amino acids are assigned values from 3 to 0 based on their polarity, hydrophobicity, shape, and charge (47). For each residue, the average biochemical similarity calculated above was compared with a simulated null model in which the nonconsensus amino acids observed in the bnAb–virus panels were randomly selected from all nonconsensus amino acids at that residue (*SI Appendix*, Fig. S5*D*). The average similarity was above the fifth percentile of the respective null model for 53% of the residues (*SI Appendix*, Fig. S5*D*), indicating that, on average, the amino acids sampled at these residues are more biochemically similar to the consensus amino acid than a uniformly selected random sample. The fact that the observed mutations are biochemically similar may explain why they did not significantly alter binding characteristics of the bnAbs. We then computed the fitness cost for the observed mutations at these residues and compared them with the mutations that were not observed as before. We expect that the latter mutations to biochemically different amino acids may have affected IC-50, but did not arise in viable viruses because of their high fitness costs; that is, the fitness cost associated with evolving escape mutations was prohibitive. Consistent with this expectation, our fitness landscape predicts that the fitness cost for the

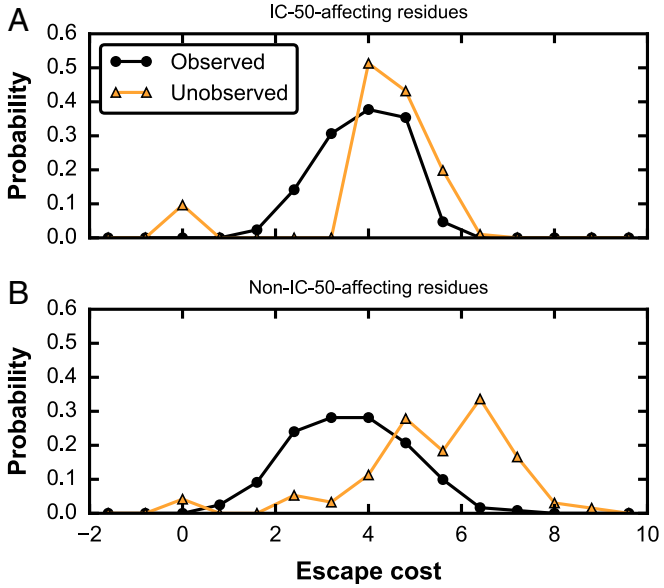

Fig. 5. Distribution of fitness costs for residues in the footprints of CD4bs-directed bnAbs. The footprint residues for a set of CD4bs-directed bnAbs (listed in *SI Appendix*, *Text 7*) were determined using crystal structures (as described in *SI Appendix*, *Text 7*). Next, the CATNAP online tool (43), a database of experimental IC-50 measurements between panels of bnAb–virus pairs, was used to identify amino acids within these footprints that are statistically associated with either high or low IC-50 for the bnAb–virus pairs tested. The footprint residues were separated into two sets of residues: the first set (*A*) consists of those residues for which at least one amino acid is statistically associated with a change in IC-50; the second set (*B*) consists of all other residues in the footprint where no such statistical associations with IC-50 were found. For both graphs, the fitness costs are calculated over all amino acids present in the CATNAP bnAb–virus panels (observed) and all amino acids not present in these CATNAP panels (unobserved). For the residues in *A*, the means of the observed and unobserved fitness cost distributions are 3.86 and 4.17, respectively ($P < 0.001$); for the residues in *B*, the means of the observed and unobserved fitness cost distributions are 3.61 and 5.42, respectively ($P < 0.001$); the *P* values were estimated by simulating from a null model in which the amino acids that were observed or unobserved are randomly permuted for each residue in the footprint.

observed mutations are lower than those for the unobserved mutations (Fig. 5*B*).

bnAbs That Target the CD4 Binding Site Contact Select Residues That Are Predicted to Be Associated with a High Fitness Cost upon Mutation. We computed the fitness cost associated with making mutations at all gp160 residues by carrying out Monte Carlo simulations to obtain an ensemble of sequences, all of which contained the consensus amino acid at a chosen residue. This ensemble of sequences was used to estimate the fitness cost for each particular mutation from consensus to a nonconsensus residue, as in Eq. **5** above. The results were then averaged over the mutant amino acids (24) to weight more likely mutations more highly as shown below:

$$\overline{\Delta E_i} = \frac{\sum_{a=1}^{\tilde{q}_i} \Delta E_{i,\mathbf{h}_f,\mathbf{J}_f}(a) \exp\left[-\Delta E_{i,\mathbf{h}_f,\mathbf{J}_f}(a)\right]}{\sum_{a=1}^{\tilde{q}_i} \exp\left[-\Delta E_{i,\mathbf{h}_f,\mathbf{J}_f}(a)\right]} \qquad [6]$$

where $\tilde{q}_i$ is the number of mutants at residue i after mutant combining (*SI Appendix*, *Text 2*). Eq. **6** provides us with an average fitness cost of evolving mutations at a particular residue, i, averaged over all sequence backgrounds in which the mutation might arise and over all mutant amino acids. We then superimposed this predicted residue-level fitness costs onto the SOSIP crystal structure. This can be visualized in a heat map depicting the fitness costs of residues that we determined to be accessible on the surface of SOSIP (Fig. 6*A*) (*SI Appendix*, *Text 6*). These results show that the map is very rugged, composed of a mixture of closely spaced low- and high-fitness cost residues. To obtain a clearer picture of whether low-fitness cost residues are predominant in any region of the size of a typical antibody footprint, we calculated the fitness cost (*SI Appendix*, Eq. **S24**) averaged over all surface residues within 12.5 Å of the chosen residue (the radius of a typical antibody footprint, as estimated from analyzing various bnAb–gp160 crystal structures). The corresponding heat map shows that fitness costs averaged over the antibody footprint are smooth over the entire surface on this scale (Fig. 6*B*). Ab-footprint–sized regions are typically dominated by low-fitness cost residues. Thus, most Ab responses that arise may be escaped via mutations. Even though the CD4 binding site has one of the largest fitness costs when averaged over a typical antibody footprint size (Fig. 6*B*), there still exist several residues associated with low fitness costs for mutations. Hence, if mutations at these residues lead to abrogation of Ab binding, then they present relatively easy escape pathways for the virus, consistent with the previous observation based on CATNAP data. We note that two other regions in Fig. 6*A* appear to have large numbers of high-escape cost residues: (*i*) the $\alpha 0$ and $\beta\bar{1}$ motifs of the C1 region of gp120, located in the trimer core near the intertrimer interfaces as well as the gp120–gp41 interface (48), and (*ii*) a region of gp41 containing portions of the H2 and membrane-proximal external region (MPER) motifs (49–52), although much of the MPER region is truncated in the 5D9Q crystal structure, including the epitopes for MPER-directed bnAbs 2F5 and 4E10 (51). However, the first region is sterically inaccessible to antibodies, while the second region contains a few highly variable residues that dominate the averaging in Eq. **6**, and thus on the scale of a footprint it is not very conserved.

We next examined the residues in the CD4 binding site region that are most strongly associated with the binding of the VRC01 class of antibodies. Li et al. (53) created an extensive set of alanine scanning mutants on a background of JRCSF, a CCR5-tropic clade B gp160 strain. For each alanine mutant, the authors measured binding affinity of full-length gp120 monomer to VRC01 relative to the wild-type virus. This assay led to the identification of residues where mutation to alanine led to significant decrease in VRC01–gp120 binding. The authors additionally conducted a neutralization assay in which whole mutant pseudoviruses are incubated with live target cells, and loss of infectivity is measured as a function of concentration of added CD4–Ig, a synthetic construct in which the CD4 domains 1 and 2 are fused to human IgG1 Fc domain. CD4–Ig competes with target cells to bind to the CD4 binding site of the pseudovirus, thus hindering infection of target cells. In this assay, if lower concentrations of CD4–Ig are required to inhibit infection, a decreased ability of the alanine mutant to infect via CD4-mediated interactions is indicated. In other words, a viral strain with a low CD4–Ig value has a low replicative fitness. The portion of these data corresponding to the gp160 residues in contact with VRC01 can be determined from crystal structures (*SI Appendix*, Table S5).

Of the residues on gp160 that were determined to be important for binding to VRC01, seven of these result in significant loss of binding (<33%) to gp120 upon mutation to alanine. While three of these seven (367, 368, and 457) are predicted by our landscape to have high fitness cost upon mutation, the remaining four (279, 371, 467, and 474) have much lower predicted fitness cost. This is seemingly at odds with the apparent high fitness cost of mutation to alanine for all seven residues, as measured experimentally (loss in sensitivity to CD4–Ig neutralization). This discrepancy can likely be explained by examining these residues at the amino acid level. For the four residues in question, the most common nonconsensus amino acid accounts for a large fraction of sequences in the MSA (*SI Appendix*, Fig.

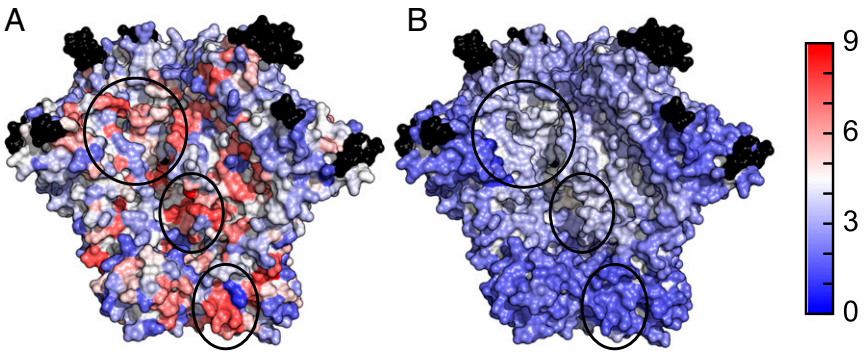

Fig. 6. Fitness costs superimposed on SOSIP Env gp160 trimer (PDB ID code 5D9Q). High-fitness cost residues (red) are more difficult for the virus to mutate, while low-fitness cost residues (blue) tend to be highly variable and easy to mutate. Residues in black are considered hypervariable and are not included in our model. (*A*) Fitness cost for each residue is averaged over all possible sequence backgrounds and amino acids at that residue. (*B*) Additionally averaged over surface residues within 12.5 Å of the residue. In both *A* and *B*, the regions circled in black, from *Top Left* to *Bottom Right*, correspond to the CD4bs, the $\alpha 0$ and $\beta\bar{1}$ motifs of the C1 region of gp120, and a region of gp41 containing portions of the H2 and MPER motifs, respectively.

S6), and it is not alanine. Thus, mutation to the most common nonconsensus amino acid is unlikely to result in a high fitness cost. Furthermore, in the CATNAP panel described in the previous section, neither the consensus nor the most common mutant amino acid is significantly associated with change in IC-50. Rather, the distributions of IC-50s for sequences containing either the consensus or the most common mutant amino acid are indistinguishable by two-tailed *t* test (*SI Appendix*, Fig. S6). This evidence suggests that mutation to the most common mutant amino acid may be insufficient to abrogate binding to VRC01. Our predicted fitness costs are likely artificially low, since Eq. **6** tends to weight low-fitness cost amino acid mutations highly during the averaging procedure and we infer that mutation to the most common nonconsensus amino acid does not incur a high fitness cost. If we instead calculate the fitness costs for these residues specifically to alanine, we predict much higher values (3.7, 4.2, 2.7, and 4.7, for residues 279, 371, 467, and 474, respectively). In contrast, for the three residues with high predicted fitness cost, the frequency of the most-common mutant amino acid was at most 0.2% in the MSA. Thus, although alanine was not the most-common mutant, the experimental fitness measurements made using alanine mutants were representative of typical escape costs at these residues. Most convincingly, 9 out of the top 10 residues with largest predicted fitness cost had an undetectable CD4–Ig value (*SI Appendix*, Table S5), further suggesting that our landscape provides an accurate measure of intrinsic fitness.

These results show that, consistent with observations regarding the VRCO1 class of antibodies, our fitness landscape predicts that bnAbs that target the CD4 binding-site region selectively bind to those residues associated with the largest fitness costs. They furthermore highlight the importance of describing fitness at the amino acid level of detail, not just residues—a fact that further highlights the importance of the fitness landscape that we have inferred.

Discussion

HIV is a highly mutable virus, and the design of both T cell and antibody arms of an effective vaccine would benefit from a knowledge of its mutational vulnerabilities as this would identify targets on the HIV proteome and viral spike where potent immune responses should be directed. Determining the fitness of the virus (ability to assemble, replicate, and propagate infection) as a function of the sequence of its proteins would help in this regard. Because of the significance of compensatory or deleterious coupling between mutations at multiple residues, in determining such a fitness landscape, it is important to account for the effects of coupling between mutations. Past work has been reasonably successful in determining such a fitness landscape for diverse HIV polyproteins by inferring the same from sequence data and testing predictions against in vitro experiments and clinical data (19, 22–25). This has not been true for the gp160 Envelope polyprotein that forms the virus's spike and is targeted by antibodies. This is due to the large diversity and size of gp160 (Fig. 1). We have reported a computational approach, based on the maximum-entropy method (19, 22), which includes a data-driven parameter reduction method, an initial estimation of the prevalence landscape parameters based on the principle of MPF, followed by a BML procedure to refine the parameters (Fig. 2). We applied this framework to infer the fitness landscape of gp160 from available sequence data. Predictions of the resulting model compare very well with published experimental data, including intrinsic fitness measurements, protein contacts in the SOSIP trimer, and known escape mutations that arise to evade antibodies that target the CD4 binding site.

A natural question, equally valid for any viral protein, is why one may see a strong relation between prevalence and fitness, and what are the fundamental processes underpinning this relationship. Motivated by this question, for internal HIV proteins that are targeted by cytotoxic T lymphocytes (CTLs), a mechanistic explanation has been proposed on the basis of simulation studies of HIV evolution and associated theory (22, 23, 26). Three key factors were identified for HIV proteins: (*i*) Because of the huge diversity of HLA genes in the population, very few regions of the HIV proteome are targeted by a significant fraction of humans. (*ii*) If a mutation is forced by the immune response of a particular individual and it incurs a fitness cost, then upon infection of a new patient who does not target the same region, during chronic infection the first mutation will revert. (*iii*) Unlike influenza, the HIV population has not been subjected to a few effective classes of natural or vaccine-induced immune responses by a significant fraction of humans across the world. Therefore, it has not evolved in narrowly directed ways to evade effective herd memory responses. (*iv*) Furthermore, the effects of phylogeny are ameliorated due to high rates of recombination (54). For these reasons, over reasonable mutational distances, HIV proteins are in a steady state and so amenable to inference of fitness landscapes using maximum-entropy approaches applied to sequence data. This is decidedly not true for the influenza population, which is driven far out of equilibrium (55, 56). The first of the above arguments, however, does not translate directly to gp160, which is primarily targeted by antibodies (57). While it is tempting to draw high-level analogies with the CTL-based phenomena on the basis that the diversity of antibodies generated against HIV is large, there are clear distinctions. For example, it is known that the V2 loop of

gp160 is estimated to be immunogenic in 20–40% of infected patients, while the V3 loop induces antibodies in essentially all infected patients (58). This would seem to promote more directed evolution compared with the internal proteins under CTL pressure. However, it is possible that different individuals evolve antibodies that target different residues in the V2 and V3 loops. It is also true that peptides derived from gp160 are targeted by CTLs, and that antibody responses are often directed toward debris from the fragile HIV spike. These reasons may underlie why we see excellent correspondence between our inferred model for gp160 and experimental measurements. Nonetheless, the mechanistic reasons remain unclear for gp160. Resolving these basic principles governing the strong prevalence–fitness correspondences identified in this paper for gp160 is worthy of future study.

We also considered an optimized model using the fields only, obtained by fitting only the single-mutant probabilities. We observe a modest gain in using the model with couplings, compared with the fields model; that is, the fields model has a correlation of $\overline{\rho} = -0.69$ compared with the correlation of $\overline{\rho} = -0.74$ using our computational framework.

The reason the comparison with in vitro fitness measurements is not much worse for the model with fields only is because the coupling matrix is relatively sparse, and so unless fitness measurements are carried out with only the subset of mutants with large couplings, the fields are dominant. No such preselection was done in the data on in vitro fitness that we compared our predictions against. The value of the coupling parameters is seen in several contexts. For example, protein contacts simply cannot be predicted without the couplings because the physical interactions between these residues induce a correlated mutation structure. More importantly, the fitness consequences of the couplings can be very significant for the evolution of HIV in vivo (the situation of ultimate interest), as described below.

Barton et al. (24) studied a cohort of HIV-infected individuals and used the inferred fitness landscapes of HIV proteins (other than gp120) to predict how long it took for the virus to escape from the initial T cell immune pressure in individual patients. When using single-residue entropy alone (i.e., fields only), there was only a 15% correlation between single-residue conservation and escape time. However, when they carried out dynamic simulations of the evolution using the fitness landscape that includes coupling parameters, this correlation was 72% and statistically significant. The reason for this dramatic increase in performance upon including the couplings is that evolutionary trajectories in vivo can sample many potential compensatory pathways that may aid escape due to the high rate of replication and mutation of HIV. Therefore, pathways characterized by particularly strong compensatory couplings can be accessed. Similarly, Barton et al. (24) showed that dramatic differences in escape time for patients targeting the same epitope could be explained by differences in the background mutations contained in the sequence of the virus strains that infected these patients. For example, if the background mutations had strong negative couplings with the ultimate escape mutation, the escape mutation took much longer to evolve and take over the population. Therefore, in the context of the real in vivo situation of interest, including the couplings is very significant. This point has also been emphasized in other contexts where compensatory mutations have been observed (16–18, 59, 60).

While our method was developed to address the specific challenges posed by the gp160 protein, the approach is general and may be applied to other high-dimensional maximum-entropy inference problems. For example, it may be directly applied to estimate the prevalence landscape of other HIV proteins, or proteins of other viruses. As an example, we applied the framework to p24, a relatively conserved internal protein of HIV. The landscape with ~80,000 parameters was inferred very quickly (~2.3 h for MPF and 1.2 h for the subsequent BML), and predictions from this landscape compared favorably with experimental fitness values (19), returning a strong Spearman correlation of −0.8 (*SI Appendix*, Fig. S2). For p24, along with other HIV proteins, similar correspondences between prevalence and fitness have been obtained through other maximum-entropy inference methods (19, 22–24).

We showed that the fitness landscape of the surface-accessible parts of the ENV trimer is very rugged where a few residues that incur a large fitness cost upon mutation (including the effects of couplings between mutations) are surrounded by residues with a low fitness cost upon mutation (Fig. 6). Even for the relatively "conserved" CD4 binding-site region, only mutations at some residues are predicted to incur large fitness costs upon mutations. This is consistent with the coarse-grained models of antibody–virus binding employed in models of affinity maturation with variant antigens by Wang et al. (61) and Shaffer et al. (62). In contrast, in a related study, Luo and Perelson (62, 63) assumed that variant antigens contain epitopes composed of only conserved or only variable residues. Our observation about the spatial distribution of escape costs on the surface of HIV envelope suggests that antibody footprints will in general contain both conserved and variable residues. It is likely that these conserved residues need to be the principal targets of effective antibody responses that are difficult for the virus to evade. For this reason, the availability of our fitness landscape of HIV's envelope proteins is expected to aid the rational design of immunogens that could potentially induce bnAbs upon vaccination (1–7), as well as guide the choice of combination of known bnAbs that would prevent escape in humans undergoing passive antibody therapy (10).

Specifically, our fitness landscape can be clinically useful in the future for the selection of combination bnAb therapy. Much like in the realm of antiretroviral drugs, the use of multiple different bnAbs has the potential to prevent or delay escape mutations, as the viruses in the host must evolve escape mutations in combinations of binding sites of the bnAbs administered. Two bnAbs with epitopes that have many detrimental couplings between them in all possible sequence backgrounds are likely to delay escape in diverse patients with different virus strains due to the added difficulty of introducing simultaneous escape mutations in both epitopes. Furthermore, bnAbs that target epitopes containing residues wherein escape mutations can be easily compensated by other mutations should be avoided. The importance of considering the fitness landscape in an analogous context of antiretroviral drugs has been previously shown for protease by Butler et al. (25).

An additional application that is clinically relevant is the selection of variant antigens (e.g., variants of SOSIP) for use in a candidate HIV vaccine designed to elicit bnAbs. The induction of bnAbs via vaccination will likely require immunization with multiple variant antigens that share some conserved residues, but whose variable regions contain distinct mutations compared with each other. The fitness landscape inferred in this work can provide insight into which residues within these antigens should be mutated within candidate immunogens such that the induced bnAbs are cross-reactive to diverse circulating viral strains with different sequences.

Materials and Methods

SI Appendix, Text includes detailed descriptions of the data preprocessing (*SI Appendix, Text 1*), computational framework (*SI Appendix, Text 2*), fitness verification (*SI Appendix, Text 3*), residue contact prediction (*SI Appendix, Text 4*), comparison with other methods (*SI Appendix, Text 5*), and application of the landscape for characterizing the fitness cost of escape mutations from bnAbs (*SI Appendix, Text 6–8*). The landscape, processed MSA, and implementation of the computational framework are freely available on the following website: https://github.com/raymondlouie/MPF-BML.

ACKNOWLEDGMENTS. This research was funded by the Ragon Institute of Massachusetts General Hospital, Massachusetts Institute of Technology, and Harvard (to K.J.K., J.P.B., and A.K.C.), the Hong Kong Research Grant Council General Research Fund with Project 16207915 (to R.H.Y.L. and M.R.M.), and a Harilela endowment (to M.R.M.).

1. Kwong PD, Mascola JR, Nabel GJ (2013) Broadly neutralizing antibodies and the search for an HIV-1 vaccine: The end of the beginning. *Nat Rev Immunol* 13:693–701.
2. Burton DR, et al. (2012) A blueprint for HIV vaccine discovery. *Cell Host Microbe* 12: 396–407.
3. Klein F, et al. (2013) Somatic mutations of the immunoglobulin framework are generally required for broad and potent HIV-1 neutralization. *Cell* 153:126–138.
4. Mascola JR, Haynes BF (2013) HIV-1 neutralizing antibodies: Understanding nature's pathways. *Immunol Rev* 254:225–244.
5. Szabo FK, Hoffman GE (2014) Autoreactivity in HIV-1 broadly neutralizing antibodies: Implications for their function and induction by vaccination. *Curr Opin HIV AIDS* 9: 224–234.
6. Verkoczy L, et al. (2013) Induction of HIV-1 broad neutralizing antibodies in 2F5 knock-in mice: Selection against membrane proximal external region-associated autoreactivity limits T-dependent responses. *J Immunol* 191:2538–2550.
7. Zolla-Pazner S (2014) A critical question for HIV vaccine development: Which antibodies to induce? *Science* 345:167–168.
8. Hansen SG, et al. (2011) Profound early control of highly pathogenic SIV by an effector memory T-cell vaccine. *Nature* 473:523–527.
9. Hansen SG, et al. (2009) Effector memory T cell responses are associated with protection of rhesus monkeys from mucosal simian immunodeficiency virus challenge. *Nat Med* 15:293–299.
10. Lu CL, et al. (2016) Enhanced clearance of HIV-1-infected cells by broadly neutralizing antibodies against HIV-1 in vivo. *Science* 352:1001–1004.
11. Barouch DH, et al. (2013) Therapeutic efficacy of potent neutralizing HIV-1-specific monoclonal antibodies in SHIV-infected rhesus monkeys. *Nature* 503:224–228.
12. Klein F, et al. (2012) HIV therapy by a combination of broadly neutralizing antibodies in humanized mice. *Nature* 492:118–122.
13. Haddox HK, Dingens AS, Bloom JD (2017) Experimental estimation of the effects of all amino-acid mutations to HIV's envelope protein on viral replication in cell culture. *PLoS Pathog* 12:e1006114.
14. Allen TM, et al. (2005) Selective escape from $CD8^+$ T-cell responses represents a major driving force of human immunodeficiency virus type 1 (HIV-1) sequence diversity and reveals constraints on HIV-1 evolution. *J Virol* 79:13239–13249.
15. Ferrari G, et al. (2011) Relationship between functional profile of HIV-1 specific CD8 T cells and epitope variability with the selection of escape mutants in acute HIV-1 infection. *PLoS Pathog* 7:e1001273.
16. Troyer RM, et al. (2009) Variable fitness impact of HIV-1 escape mutations to cytotoxic T lymphocyte (CTL) response. *PLoS Pathog* 5:e1000365.
17. Liu Y, et al. (2013) A sensitive real-time PCR based assay to estimate the impact of amino acid substitutions on the competitive replication fitness of human immunodeficiency virus type 1 in cell culture. *J Virol Methods* 189:157–166.
18. da Silva J, Coetzer M, Nedellec R, Pastore C, Mosier DE (2010) Fitness epistasis and constraints on adaptation in a human immunodeficiency virus type 1 protein region. *Genetics* 185:293–303.
19. Mann JK, et al. (2014) The fitness landscape of HIV-1 gag: Advanced modeling approaches and validation of model predictions by in vitro testing. *PLoS Comput Biol* 10: e1003776.
20. Doud MB, Bloom JD (2016) Accurate measurement of the effects of all amino-acid mutations on influenza hemagglutinin. *Viruses* 8:155.
21. Wu NC, et al. (2015) Functional constraint profiling of a viral protein reveals discordance of evolutionary conservation and functionality. *PLoS Genet* 11:e1005310.
22. Ferguson AL, et al. (2013) Translating HIV sequences into quantitative fitness landscapes predicts viral vulnerabilities for rational immunogen design. *Immunity* 38: 606–617.
23. Barton JP, Kardar M, Chakraborty AK (2015) Scaling laws describe memories of host-pathogen riposte in the HIV population. *Proc Natl Acad Sci USA* 112:1965–1970.
24. Barton JP, et al. (2016) Relative rate and location of intra-host HIV evolution to evade cellular immunity are predictable. *Nat Commun* 7:11660.
25. Butler TC, Barton JP, Kardar M, Chakraborty AK (2016) Identification of drug resistance mutations in HIV from constraints on natural evolution. *Phys Rev E* 93: 022412.
26. Shekhar K, et al. (2013) Spin models inferred from patient-derived viral sequence data faithfully describe HIV fitness landscapes. *Phys Rev E Stat Nonlin Soft Matter Phys* 88: 062705.
27. Figliuzzi M, Jacquier H, Schug A, Tenaillon O, Weigt M (2016) Coevolutionary landscape inference and the context-dependence of mutations in beta-lactamase TEM-1. *Mol Biol Evol* 33:268–280.
28. Mora T, Walczak AM, Bialek W, Callan CG, Jr (2010) Maximum entropy models for antibody diversity. *Proc Natl Acad Sci USA* 107:5405–5410.
29. Cocco S, Monasson R (2011) Adaptive cluster expansion for inferring Boltzmann machines with noisy data. *Phys Rev Lett* 106:090601.
30. Barton JP, De Leonardis E, Coucke A, Cocco S (2016) ACE: Adaptive cluster expansion for maximum entropy graphical model inference. *Bioinformatics* 32:3089–3097.
31. Sohl-Dickstein J, Battaglino P, DeWeese MR (2011) Minimum probability flow learning. *Proceedings of the 28th International Conference on Machine Learning* (International Machine Learning Society, Bellevue, WA), pp 905–912.
32. Barton J, Cocco S (2013) Ising models for neural activity inferred via selective cluster expansion: Structural and coding properties. *J Stat Mech Theory Exp* 2013:P03002.
33. Riedmiller M, Braun H (1993) A direct adaptive method for faster backpropagation learning: The RPROP algorithm. *IEEE International Conference on Neural Networks* (Institute of Electrical and Electronics Engineers, Piscataway, NJ), pp 586–591.
34. Lobritz MA, Marozsan AJ, Troyer RM, Arts EJ (2007) Natural variation in the V3 crown of human immunodeficiency virus type 1 affects replicative fitness and entry inhibitor sensitivity. *J Virol* 81:8258–8269.
35. Anastassopoulou CG, et al. (2007) Escape of HIV-1 from a small molecule CCR5 inhibitor is not associated with a fitness loss. *PLoS Pathog* 3:e79.
36. Kassa A, et al. (2009) Identification of a human immunodeficiency virus type 1 envelope glycoprotein variant resistant to cold inactivation. *J Virol* 83:4476–4488.
37. Weigt M, White RA, Szurmant H, Hoch JA, Hwa T (2009) Identification of direct residue contacts in protein-protein interaction by message passing. *Proc Natl Acad Sci USA* 106:67–72.
38. Morcos F, et al. (2011) Direct-coupling analysis of residue coevolution captures native contacts across many protein families. *Proc Natl Acad Sci USA* 108:E1293–E1301.
39. Gueudré T, Baldassi C, Zamparo M, Weigt M, Pagnani A (2016) Simultaneous identification of specifically interacting paralogs and interprotein contacts by direct coupling analysis. *Proc Natl Acad Sci USA* 113:12186–12191.
40. Bitbol A-F, Dwyer RS, Colwell LJ, Wingreen NS (2016) Inferring interaction partners from protein sequences. *Proc Natl Acad Sci USA* 113:12180–12185.
41. Jardine JG, et al. (2016) Minimally mutated HIV-1 broadly neutralizing antibodies to guide reductionist vaccine design. *PLoS Pathog* 12:1–33.
42. Sullivan N, et al. (1998) CD4-induced conformational changes in the human immunodeficiency virus type 1 gp120 glycoprotein: Consequences for virus entry and neutralization. *J Virol* 72:4694–4703.
43. Yoon H, et al. (2015) CATNAP: A tool to compile, analyze and tally neutralizing antibody panels. *Nucleic Acids Res* 43:W213–W219.
44. Klein F, et al. (2012) Broad neutralization by a combination of antibodies recognizing the CD4 binding site and a new conformational epitope on the HIV-1 envelope protein. *J Exp Med* 209:1469–1479.
45. Shingai M, et al. (2013) Antibody-mediated immunotherapy of macaques chronically infected with SHIV suppresses viraemia. *Nature* 503:277–280.
46. McLachlan AD (1972) Repeating sequences and gene duplication in proteins. *J Mol Biol* 64:417–437.
47. Sneath PHA (1966) Relations between chemical structure and biological activity in peptides. *J Theor Biol* 12:157–195.
48. Pancera M, et al. (2010) Structure of HIV-1 gp120 with gp41-interactive region reveals layered envelope architecture and basis of conformational mobility. *Proc Natl Acad Sci USA* 107:1166–1171.
49. Huang J, et al. (2014) Broad and potent HIV-1 neutralization by a human antibody that binds the gp41-gp120 interface. *Nature* 515:138–142.
50. Sun ZYJ, et al. (2008) HIV-1 broadly neutralizing antibody extracts its epitope from a kinked gp41 ectodomain region on the viral membrane. *Immunity* 28:52–63.
51. Krebs SJ, et al. (2014) Multimeric scaffolds displaying the HIV-1 envelope MPER induce MPER-specific antibodies and cross-neutralizing antibodies when co-immunized with gp160 DNA. *PLoS One* 9:e113463.
52. Julien J-P, et al. (2013) Crystal structure of a soluble cleaved HIV-1 envelope trimer. *Science* 342:1477–1483.
53. Li Y, et al. (2011) Mechanism of neutralization by the broadly neutralizing HIV-1 monoclonal antibody VRC01. *J Virol* 85:8954–8967.
54. Neher RA, Russell CA, Shraiman BI (2014) Predicting evolution from the shape of genealogical trees. *Elife* 3:1–18.
55. Neher RA, Bedford T, Daniels RS, Russell CA, Shraiman BI (2016) Prediction, dynamics, and visualization of antigenic phenotypes of seasonal influenza viruses. *Proc Natl Acad Sci USA* 113:E1701–E1709.
56. Luksza M, Lässig M (2014) A predictive fitness model for influenza. *Nature* 507:57–61.
57. Overbaugh J, Morris L (2012) The antibody response against HIV-1. *Cold Spring Harb Perspect Med* 2:a007039.
58. Zolla-Pazner S, Cardozo T (2010) Structure-function relationships of HIV-1 envelope sequence-variable regions refocus vaccine design. *Nat Rev Immunol* 10:527–535.
59. Brockman MA, et al. (2007) Escape and compensation from early HLA-B57-mediated cytotoxic T-lymphocyte pressure on human immunodeficiency virus type 1 Gag alter capsid interactions with cyclophilin A. *J Virol* 81:12608–12618.
60. Martinez-Picado J, et al. (2006) Fitness cost of escape mutations in p24 Gag in association with control of human immunodeficiency virus type 1. *J Virol* 80:3617–3623.
61. Wang S, et al. (2015) Manipulating the selection forces during affinity maturation to generate cross-reactive HIV antibodies. *Cell* 160:785–797.
62. Shaffer JS, Moore PL, Kardar M, Chakraborty AK (2016) Optimal immunization cocktails can promote induction of broadly neutralizing Abs against highly mutable pathogens. *Proc Natl Acad Sci USA* 113:E7039–E7048.
63. Luo S, Perelson AS (2015) Competitive exclusion by autologous antibodies can prevent broad HIV-1 antibodies from arising. *Proc Natl Acad Sci USA* 112:11654–11659.

SI Text

1) Data preprocessing.

We downloaded the amino acid multiple sequence alignment (MSA) of HIV-1 Clade B gp160 sequences from the Los Alamos National Laboratory (LANL) HIV sequence database (www.hiv.lanl.gov; accessed 14th May, 2016). To control sequence quality, we excluded sequences (i) labeled by LANL as 'problematic', (ii) with ≥ 2% gaps at non hyper-variable residues (https://www.hiv.lanl.gov/content/sequence/VAR_REG_CHAR/variable_region_characterization_explanation.html), (iii) with > 10 consecutive insertions at residues where there is an amino acid at every other sequence or (iv) which are outliers as determined by principal component analysis (PCA) (as described in (1)). We then removed sequences labeled or predicted to be CXCR4-tropic, where the prediction was performed using (2). A total of 20043 sequences remained after excluding the above sequences, with these sequences belonging to a total of 1918 patients.

To control residue quality, we excluded residues which are (i) 100% conserved, (ii) contain >90% gaps or are ambiguous, or (iii) are in the hyper-variable regions due to the poor quality of the alignment. We then included eight additional "artificial" residues whose states reflect the number of residues and N-linked glycans in the four hyper-variable regions we have excluded. This resulted in a total of L=815 residues. The ambiguous residues were then imputed with a simple mean imputation. The MSA can be represented by a matrix $\mathbf{X}$ where the lth row is a vector of amino acids $\mathbf{x}_\ell = [x_{\ell 1}, \ldots, x_{\ell L}]$ representing the lth sequence, where the amino acids at residue i are identified as either consensus ($x_{\ell i} = 0$) or the kth dominant (most frequent) mutant ($x_{\ell i} = k$), for $k=1,..,\ q_i$ where q_i denotes the number of mutants at residue i.

2) Computational model and framework

2.1 Maximum entropy model. We consider a probabilistic model designed to reproduce the single and double mutant probabilities

$$f_i(a) = \frac{1}{P}\sum_{k=1}^{B} w_k \delta(x_{ki}, a) \qquad \text{(S1)}$$

$$f_{ij}(a,b) = \frac{1}{P}\sum_{k=1}^{B} w_k \delta(x_{ki}, a)\delta(x_{kj}, b)$$

where $f_i(a)$ denotes the frequency of amino acid a at residue i and $f_{ij}(a,b)$ the joint frequency of amino acids a and b at residues i and j respectively, as observed from the MSA $\mathbf{X}$. Also, B is the number of sequences after data preprocessing, δ is the Kronecker delta function

$$\delta(a,b) = \begin{cases} 0 & \text{if } a \neq b \\ 1 & \text{if } a = b \end{cases}, \qquad \text{(S2)}$$

P=1918 is the number of patients, and w_k is one divided by the number of MSA sequences contributed by the patient from which sequence k was extracted. The weights w_k ensure that the different number of sequences extracted per patient do not bias the calculation of the single and double mutant probabilities.

A vast family of probabilistic models can reproduce the single and double mutant probabilities in Eq. S1. Among such models, we consider the 'least biased' model that maximizes the entropy of the sequence distribution. For a given sequence $\mathbf{x} = [x_1, x_2, \ldots, x_L]$, this maximum entropy model assigns the probability

$$p_{\mathbf{h},\mathbf{J}}\left(\mathbf{x}\right)=\frac{\exp\left(-E_{\mathbf{h},\mathbf{J}}\left(\mathbf{x}\right)\right)}{Z} \tag{S3}$$

$$E_{\mathbf{h},\mathbf{J}}\left(\mathbf{x}\right)=\sum_{i=1}^{L}h_i\left(x_i\right)+\sum_{i=1}^{L}\sum_{j=i+1}^{L}J_{ij}\left(x_i,x_j\right) \tag{S4}$$

where **h** denotes the set of all fields, **J** denotes the set of all couplings, Z is the partition function (a normalization ensuring the distribution has total mass of unity), while $E(\mathbf{x})$ is the "energy" of strain **x**. The field $h_i(x_i)$ and coupling $J_{ij}(x_i, x_j)$ parameters are chosen such that the single and double mutant probabilities of the model match those in the data, i.e.,

$$f_i\left(a\right)=\sum_{\mathbf{x}}\delta\left(x_i,a\right)\ p_{\mathbf{h},\mathbf{J}}\left(\mathbf{x}\right) \tag{S5}$$

$$f_{ij}\left(a,b\right)=\sum_{\mathbf{x}}\delta\left(x_i,a\right)\delta\left(x_j,b\right)\ p_{\mathbf{h},\mathbf{J}}\left(\mathbf{x}\right).$$

This choice can be formulated as the following convex optimization problem (see e.g (3))

$$\left(\mathbf{h}^*,\mathbf{J}^*\right)=\arg\min_{\mathbf{h},\mathbf{J}}\mathrm{KL}\left(p_0\parallel p_{\mathbf{h},\mathbf{J}}\right) \tag{S6}$$

where

$$p_0\left(\mathbf{x}_k\right)=\frac{1}{P}\sum_{k=1}^{B}w_k\,p_{\mathbf{X}}\left(\mathbf{x}_k\right)$$

with $p_{\mathbf{X}}\left(\mathbf{x}_k\right)$ denoting the frequency of observing strain $\mathbf{x}_k$, (i.e., the fraction of rows in $\mathbf{X}$ corresponding to $\mathbf{x}_k$) and

$$\mathrm{KL}\left(p_0\parallel p_{\mathbf{h},\mathbf{J}}\right)=\sum_{\mathbf{x}}p_0\left(\mathbf{x}\right)\ \ln\ \frac{p_0\left(\mathbf{x}\right)}{p_{\mathbf{h},\mathbf{J}}\left(\mathbf{x}\right)}\ . \tag{S7}$$

This represents the Kullback-Leibler divergence between p_0 and $p_{\mathbf{h},\mathbf{J}}$.

Although the optimization problem in Eq. S6 is convex and thus can be solved by BML algorithms, the number of mutants and length of HIV proteins can be large (Fig. 1) leading to two related computational issues. First, it yields a very large number of parameters, resulting in a slow convergence. Specifically, the number of fields to be estimated is $\sum_{i=1}^{L}q_i$ while the number of couplings is $\sum_{i=1}^{L}q_i\sum_{j=i+1}^{L}q_j$. Thus the total number of parameters is given by $\sum_{i=1}^{L}\left(q_i+1\right)\sum_{j=i+1}^{L}q_j$, which can be very large for HIV, as shown in Fig. 1. This is most extreme for gp160, which has about an order of magnitude more parameters than every other protein.

Secondly, calculating the gradient required by BML algorithms can be computationally prohibitive due to the large number of terms in the partition function. Specifically, the partition involves $\prod_{i=1}^{L}\left(q_i+1\right)$ terms, which increases exponentially with the number of residues L. This makes exact computation intractable, and therefore necessitates the use of MCMC simulations to approximate the gradient. For gp160 however, proper initialization of the algorithm is essential otherwise the running time is prohibitive. To alleviate these two problems, we first reduce the number of mutants that are modeled explicitly, then apply a method to find an accurate estimate of the parameters used to initialize the BML algorithm.

2.2 Reducing the number of mutants that are explicitly modeled. To limit overfitting and to reduce the number of mutants that we consider per residue, we group the low-frequency mutants together. Specifically, we model only the top k_i most frequent mutants, whilst grouping the remaining $q_i - k_i$ mutants, such that the corresponding entropy with grouping achieves a certain fraction ϕ of the entropy without grouping (4). Mathematically, for residue *i*, this involves choosing the smallest integer k_i such that

$$S_i(k_i) \geq \phi S_i(q_i) \tag{S8}$$

where

$$S_i(k_i) = -\sum_{a=0}^{k_i} f_i(a) \ln f_i(a) - \overline{f}_i \ln \overline{f}_i \tag{S9}$$

and

$$\overline{f}_i = \sum_{a=k_i+1}^{q_i} f_i(a) \quad . \tag{S10}$$

To choose ϕ, we introduce the measure

$$\beta_i(\phi) = \frac{\sum_{a=1}^{q_i} \left(f_i(a) - \overline{f}_i(a) \right)^2}{\sum_{a=1}^{q_i} \frac{f_i(a)\left(1 - f_i(a)\right)}{P}} \tag{S11}$$

where

$$\overline{f}_i(a) = \begin{cases} f_i(a) & \text{if } a < k_i + 1 \\ \overline{f}_i & \text{if } a = k_i + 1 \\ 0 & \text{if } a > k_i + 1 \end{cases}$$

and we recall that *P* is the number of patients. The conceptual idea behind Eq. S11 is to introduce as much bias due to grouping (numerator) as possible within the limits afforded by the fluctuations in the amino acid frequencies (denominator). By noting that k_i is a function of ϕ, to achieve a balance between overfitting and underfitting, we choose ϕ such that the mean value of $\beta_i(\phi)$, taken over all residues *i=1,.,.L*, is approximately one. This selection criteria leads to the choice of $\phi^* = 0.95$ (Table S2), leading to a significant reduction in the number of model parameters. For this choice of ϕ, for the *i*th residue, we denote $\tilde{q}_i = k_i + 1$ as the modified number of mutants after combining, resulting in a new MSA matrix $\tilde{\mathbf{X}}$. This method, which we later validate for gp160 (Table S3), results in a six-fold reduction in the number of parameters.

2.3 Efficiently obtaining accurate initialization parameters through MPF. To obtain an efficient and accurate initialization for BML, we apply the principle of minimum probability flow (MPF). MPF was originally designed for the Ising model (5) which has two states per residue. Here, we consider however a Potts generalization, allowing for an arbitrary number of states per residue. To this end, we construct a binary MSA based on the amino acid MSA. Specifically, each amino acid at the *i*th residue is represented by $\tilde{q}_i$ binary digits. The *j*th most frequent amino acid is then represented by the $\tilde{q}_i$-bit binary representation of 2^{j-1}, and thus the consensus sequence is the all-zero vector. For example, if $\tilde{q}_i = 2$, then the consensus amino acid, most common and least common mutant are denoted respectively as 00, 01 and 10. We will denote $\mathbf{Y}$ as the binary matrix corresponding to the amino acid matrix $\tilde{\mathbf{X}}$, with *i*th row denoted by $\mathbf{y}_i$.

The key problem to solving Eq. S6 is that $p_{\mathbf{h},\mathbf{J}}$ contains the intractable partition function *Z*. The goal of MPF is to replace

$p_{\mathbf{h},\mathbf{J}}$ with an alternate probability mass function (PMF) which is also parametrized by the fields and couplings, but which results in a tractable objective problem (to obtain a low-complexity solution), and at the same time retain similar 'features' as $p_{\mathbf{h},\mathbf{J}}$ (to obtain an accurate solution). To simultaneously achieve these goals, a continuous-time Markov chain is considered whose states correspond to the $M = \prod_{i=1}^{L} (\tilde{q}_i + 1)$ possible sequences. The probability of each state at time zero is set to the empirical PMF p_0, and the master equation describing this Markov chain is given by

$$\frac{\mathrm{d}}{\mathrm{d}t} p_{\mathbf{h},\mathbf{J};t}(\mathbf{y}_i) = \sum_{j=1, j\neq i}^{M} \Gamma_{ij}\, p_{\mathbf{h},\mathbf{J};t}(\mathbf{y}_j) - \sum_{j=1, j\neq i}^{M} \Gamma_{ji}\, p_{\mathbf{h},\mathbf{J};t}(\mathbf{y}_i) \tag{S12}$$

where $p_{\mathbf{h},\mathbf{J};t}(\mathbf{y}_i)$ denotes the probability of $\mathbf{y}_i$ at time t, and with $p_{\mathbf{h},\mathbf{J};t} = p_0$. The solution is given by

$$p_{\mathbf{h},\mathbf{J};t}(\mathbf{y}_i) = \left[\exp(t\boldsymbol{\Gamma})\mathbf{p}_0\right]_i \tag{S13}$$

where $[\mathbf{y}]_i$ denotes the ith element of the vector $\mathbf{y}$. The matrix $\boldsymbol{\Gamma}$ is the $M \times M$ transition rate matrix with (i,j)th element Γ_{ij} designed such that

$$\lim_{t\to\infty} p_{\mathbf{h},\mathbf{J};t}(\mathbf{y}_i) = p_{\mathbf{h},\mathbf{J}}(\mathbf{y}_i) \tag{S14}$$

with details of this matrix given in (5). Thus for any given $\mathbf{h}$ and $\mathbf{J}$, the transition rate matrix is designed to ensure that as time increases, the PMF 'evolves' towards $p_{\mathbf{h},\mathbf{J}}$.

The next step is to choose a t which can result in a tractable optimization problem. MPF replaces $p_{\mathbf{h},\mathbf{J}}$ in Eq. S6 by $p_{\mathbf{h},\mathbf{J};t}$ with t small. This choice has the advantage that the resulting optimization problem is convex and easy to solve. The resulting KL divergence between p_0 and $p_{\mathbf{h},\mathbf{J};t}$ expanded as a Taylor series around $t=0$ results in the linear approximation:

$$\mathrm{KL}\left(p_0 \,\|\, p_{\mathbf{h},\mathbf{J};t}\right) = t\mathrm{K}_{\mathbf{h},\mathbf{J}} + o(t) \tag{S15}$$

where

$$\mathrm{K}_{\mathbf{h},\mathbf{J}} = \sum_{b=1}^{B}\sum_{i=1}^{L}\sum_{a=1}^{q_i} \mathrm{e}\,\mathrm{xp}\left(\frac{1}{2}\left(\left(2y_{b,(i-1)L+a} - 1\right)\sum_{j=1}^{L}\sum_{c=1}^{q_j} y_{b,(j-1)L+c} J_{ij}(a,c) - h_i(a)\right)\right) \tag{S16}$$

with $y_{b,n}$ denoting the (b,n)th entry of $\mathbf{Y}$.

Based on this representation, the estimate of the parameters can be found by minimizing the objective function $\mathrm{K}_{\mathbf{h},\mathbf{J}}$. To account for the fact that the number of samples per parameter is quite small, even after grouping the mutants, we introduce a L2 regularization term to the objective function. Moreoever, it is reasonable to assume that a significant proportion of the couplings are either zero or negligible, as most residues are physically seperated in the protein native state. As such, we also introduce a L1 regularization term, which enforces parameter sparsity. Including the L1 and L2 regularization terms, we obtain the following MPF proxy for the original optimization problem (Eq. S6):

$$\left(\mathbf{h}^{\mathrm{MPF}}, \mathbf{J}^{\mathrm{MPF}}\right) = \arg\min_{\mathbf{h},\mathbf{J}} \mathrm{K}_{\mathbf{h},\mathbf{J}} + \lambda_1 \sum_{i=1}^{L}\sum_{a=1}^{q_i}\sum_{j=i+1}^{L}\sum_{b=1}^{q_j} \left|J_{ij}(a,b)\right| + \lambda_2 \sum_{i=1}^{L}\sum_{a=1}^{q_i}\sum_{j=i+1}^{L}\sum_{b=1}^{q_j} J_{ij}(a,b)^2 \tag{S17}$$

where λ_1 and λ_2 are the L1 and L2 regularization parameters respectively. Note that this objective function is convex and does not contain the intractable partition function. In particular, it involves only a quadratic number of terms in $\tilde{L}$, and can be easily optimized using standard gradient descent algorithms. We run gradient descent multiple times in parallel to obtain

different field and coupling parameter sets, with each set corresponding to a different set of regularization parameters.

2.4 Refinement through BML: Each field and coupling parameter set that solves Eq. S17 is used to initialize a BML algorithm using MCMC simulations to approximate the gradient. BML was implemented by a modified RPROP algorithm (6), which was run for each parameter set. The couplings which were set to zero due to the L1 regularization in Eq. S17 were fixed to zero during each iteration of the BML algorithm. Out of these different parameter sets, we choose the one, as in (7, 8), such that

$$\varepsilon_1 = \frac{1}{\tilde{L}} \sum_{i=1}^{L} \sum_{a=1}^{\tilde{q}_i} \frac{\left(f_i^{\text{model}}(a;\lambda_1,\lambda_2) - f_i(a,\phi^*) \right)^2}{\frac{f_i(a,\phi^*)\left(1 - f_i(a,\phi^*)\right)}{P}} \approx 1$$

$$\varepsilon_2 = \frac{1}{\sum_{k=1}^{L} \tilde{q}_k \sum_{l=k+1}^{L} \tilde{q}_l} \sum_{i=1}^{L} \sum_{a=1}^{\tilde{q}_i} \sum_{j=i+1}^{L} \sum_{b=1}^{\tilde{q}_j} \frac{(f_{ij}^{\text{model}}(a,b;\lambda_1,\lambda_2) - f_{ij}(a,b,\phi^*))^2}{\frac{f_{ij}(a,b,\phi^*)\left(1 - f_{ij}(a,b,\phi^*)\right)}{P}} \approx 1 \qquad \text{(S18)}$$

where $f_i^{\text{model}}(a;\lambda_1,\lambda_2)$ and $f_{ij}^{\text{model}}(a,b;\lambda_1,\lambda_2)$ are the model single and double mutant probabilities using regularization parameters λ_1 and λ_2 using the refined parameters from BML, and $f_i(a,\phi^*)$ and $f_{ij}(a,b,\phi^*)$ are the single and double mutant probabilities after grouping with combining factor ϕ^*. Note that the condition in Eq. S18 is to ensure that the regularization parameters are chosen to balance overfitting and underfitting the single and double mutant probabilities.

2.5 Summary of computational framework: The computational framework can be summarized by the following steps:

1. Combining mutants: From the pre-processed MSA, combine the mutants according to Eq. S8, with the combining factor chosen such that the mean of Eq. S11 over all sites is approximately one. Form a new MSA based on these combined mutants.
2. Minimum probability flow: Convert this new MSA into the binary matrix **Y,** which serves as an input to the optimization problem in Eq. S17. Solve this problem by any gradient descent method to obtain a parameter set. Repeat this multiple times for different regularization parameters, to obtain multiple field and parameter sets.
3. Refinement of parameters: Run any gradient descent algorithm multiple times in parallel to solve (Eq. S6), with each time using a different parameter set from step 2. Choose the parameter set in accordance with Eq. S18.

3) Fitness verification

To verify that the inferred prevalence landscape correlates well with the fitness landscape, we compared with in vitro experimental fitness measurements from literature. These were obtained by infectivity or competition assays using CCR5-tropic strains. In Fig. S1 we plot the normalized logarithm of these fitness measurements $\ln \frac{f_i}{f_{WT}}$ vs the normalized energy $E_i - E_{WT}$ for each experiment, showing in each case a strong negative correlation. Simply calculating the Spearman correlation by aggregating the fitness measurements collated from all papers is not meaningful, as the experiments and fitness measures are not consistent across these papers. Thus to account for this inconsistency, we instead consider the average Spearman correlation, a common approach in meta-analysis (9), which calculates the weighted average of the individual Spearman correlation ρ_i, with the weights equal to the number of fitness measurements N_i, and thus given by

$$\bar{\rho} = \frac{\sum_{i=1}^{7} N_i \rho_i}{\sum_{i=1}^{7} N_i} \quad . \tag{S19}$$

To further validate our computational framework, we applied it to p24, an internal protein in HIV. The inferred prevalance landscape is observed to also have a strong correlation with in vitro experimental fitness measurements (Fig. S2), and is the relative energy of the different strains is qualitavely the same as those observed in (10). These experiments were obtained by site-directed mutagensis of single, double and triple mutations into the HIV-1 NL4-3 reference strain (10).

4) Predicting residues in contact

The couplings can also be used to infer residues which are in contact in the protein native structure, and serves as a direct verification that the inferred couplings contain useful biological information (11–13). To determine the association between residues based on the inferred couplings, we consider the Direct Information (DI) (11), a measure which only takes into account the couplings between residues, and is thus a reflection of only direct associations between residues. The DI between residues *i* and *j* is given by

$$\mathrm{DI}_{i,j} = \sum_{a=1}^{\tilde{q}_i} \sum_{b=1}^{\tilde{q}_j} f_{ij}^{\mathrm{dir}}(a\ ,b) \ln \frac{f_{ij}^{\mathrm{dir}}(a,b)}{f_i(a)\, f_j(b)} \tag{S20}$$

where

$$f_{ij}^{\mathrm{dir}}(a\ ,b) = \frac{\exp\left(J_{ij}(a,b) + \tilde{h}_i(a) + \tilde{h}_j(b)\right)}{Z_{ij}}$$

with $\tilde{h}_i(a)$ and $\tilde{h}_j(b)$ chosen such that

$$f_i(a) = \sum_{b=1}^{\tilde{q}_j} f_{ij}^{\mathrm{dir}}(a\ ,b) \tag{S21}$$

$$f_j(b) = \sum_{a=1}^{\tilde{q}_i} f_{ij}^{\mathrm{dir}}(a\ ,b)$$

and Z_{ij} is a normalization constant. To reduce the effects of sampling noise and phylogenetic effects, we then modify the DI using the standard average product correction (APC) (12), which we will refer to as DI-APC. Note that the DI-APC is only a function of the couplings, and not the fields.

As residues in contact are likely to be strongly coupled, we expect that the DI-APC between these residues to be high, assuming that our inferred couplings is correct (11). We show this to be the case in Fig. S3, which plots the true positive rate (TPR) – the fraction of contacts in the top *x* predicted pairs (based on the DI-APC) which are actually in contact based on distance between the CA atoms (based on the PDB crystal structure) – vs the top *x* pairs. We observe in all cases an excellent prediction of the contacts compared to a random prediction. There are however apparent false positives which are observed (Table S5), which may be due to conformational changes that occurs when gp160 interacts with CD4 and other co-receptors.

5) Comparison with other models. We compared the ability of our MPF-BML model to predict fitness rank ordering and protein contacts with three other computationally-efficient methods (Fig. S4): MPF without BLM refinement, a fields-only model calculated to exactly fit only the single mutant probabilities, and mean-field Direct Coupling Analysis (mfDCA) (13). We observe that our model has the largest prediction accuracy in terms of both fitness rank ordering and protein. The fields-only model does quite a good job at predicting fitness rank ordering, however it fails to predict protein contacts, whereas mfDCA does well at identifying contacts, but performs poorly at predicting fitness ordering.

6) Envelope trimer geometry and surface residues. Spatial information about the envelope trimer was obtained from

Protein Data Bank ID 5D9Q. Although this is a crystal structure of SOSIP, it is assumed that the coordinates are representative of the native gp160 structure. Each residue was assigned a center of mass as the weighted average of the coordinates of its atoms (excluding hydrogen, which is not included in the crystal structure), with weights equal to the respective atomic masses. The centers of mass were used when determining residue neighborhoods below. Each residue was also assigned a solvent accessible surface area (SASA) using the PyMOL software (www.pymol.org) get_area() function, using a 1.4 solvent radius parameter, for each residue in the crystal structure. SASA values per residue were converted to relative solvent accessibility (RSA) values by normalizing by the respective SASA values per residue in a Gly-X-Gly tripeptide construct, as published by (14). Residues with RSA >0.2, used as a threshold in (15), are considered surface residues while the remaining residues are considered "buried."

7) Fitness costs. Assuming that the prevalence landscape inferred in this work accurately reflects intrinsic fitness, a measure of the difficulty for a virus to make a certain set of mutations can be quantified by the "fitness cost," or the change in energy (Eq. S4) upon introducing these mutations. We first consider the fitness cost of a mutation from the consensus amino acid to a non-consensus amino acid at a single residue. Before presenting the expression for this, it is convenient to introduce the fitness cost for amino acid *a* at residue *i* as

$$\Delta E_{i,\mathbf{h}_\mathrm{f},\mathbf{J}_\mathrm{f}}(a) = \sum_{\mathbf{x},x_i=0} \left(E_{\mathbf{h}_\mathrm{f},\mathbf{J}_\mathrm{f}}(\mathbf{x}') - E_{\mathbf{h}_\mathrm{f},\mathbf{J}_\mathrm{f}}(\mathbf{x}) \right) p_{\mathbf{h}_\mathrm{f},\mathbf{J}_\mathrm{f}}(\mathbf{x}) \tag{S22}$$

where $\mathbf{h}_\mathrm{f}$ and $\mathbf{J}_\mathrm{f}$ represent the final parameters after BML refinement, and the summation is over all sequences $\mathbf{x}$ having the consensus amino acid ('0') at the *i*th residue. Moreover, for any given $\mathbf{x}$, we define $\mathbf{x}'$ as the corresponding strain, but with amino acid *a* at residue *i*. Thus, Eq. S22 can be intepreted as the fitness cost from the consensus amino acid to amino acid *a*, averaged over all sequence backgrounds. From this, we can then obtain the fitness cost for residue *i* obtained by averaging Eq. S22 over all non-consensus amino acids:

$$\overline{\Delta E_i} = \frac{\sum_{a=1}^{\tilde{q}_i} \Delta E_{i,\mathbf{h}_\mathrm{f},\mathbf{J}_\mathrm{f}}(a) \exp\left[-\Delta E_{i,\mathbf{h}_\mathrm{f},\mathbf{J}_\mathrm{f}}(a) \right]}{\sum_{a=1}^{\tilde{q}_i} \exp\left[-\Delta E_{i,\mathbf{h}_\mathrm{f},\mathbf{J}_\mathrm{f}}(a) \right]} \quad . \tag{S23}$$

Here, we use Boltzmann averaging to emphasize low-fitness-cost pathways.

The above expression for the fitness cost is for the case in which each residue is treated in isolation. This is now extended to the case of long length scales, in which each residue is averaged along with all surface residues within a 12.5-Angstrom radius (based on residue center-of-mass). For a residue *i*, let us denote the set of all such proximal surface residues as $\mathcal{E}_i$. Then the fitness cost is averaged over all possible mutations within the neighborhood of (and including) residue *i*, given by:

$$\overline{\Delta E_{\mathcal{E}_i}} = \frac{\sum_{j\in\mathcal{E}_i} \sum_{a=1}^{\tilde{q}_j} \Delta E_{j,\mathbf{h}_\mathrm{f},\mathbf{J}_\mathrm{f}}(a) \exp\left[-\Delta E_{j,\mathbf{h}_\mathrm{f},\mathbf{J}_\mathrm{f}}(a) \right]}{\sum_{j\in\mathcal{E}_i} \sum_{a=1}^{\tilde{q}_j} \exp\left[-\Delta E_{j,\mathbf{h}_\mathrm{f},\mathbf{J}_\mathrm{f}}(a) \right]} \quad . \tag{S24}$$

For all calculations in this work involving fitness costs, averages over sequence background were performed using an MCMC sample of 33,330 sequences, assuming all mutations are from the consensus amino acid at that residue to a non-consensus amino acid. The MCMC sample used a burn-in period of 1e7 steps and a thinning parameter of 3e3 steps.

8) CATNAP analysis. CATNAP is a tool hosted by Los Alamos HIV Database that compiles published data in the form of antibody-virus neutralization values (IC-50). We used this tool to extract all IC-50 values for any bnAb-virus pairs in which the viral sequence is known and also included in the clade B sequences used to fit our landscape; we assumed that these sequences are viable (i.e. the corresponding viruses can grow and replicate in vivo). For any particular antibody, there

exists a panel of viruses against which the IC-50 has been measured. CATNAP uses Fisher's exact test (16) to determine whether any particular amino acids at any residue are statistically associated with either high or low IC-50 in the viral panel. We tagged any such residue as "IC-50-affecting." In other words, mutations at these binding-associated residues can potentially allow a bnAb that previously did not bind to the virus to bind upon mutation, or vice versa. Thus, these residues are likely candidates for escape from antibody pressure.

The CATNAP tool was used to analyze binding properties of the following antibodies: 10-1074, 1B2530, 8ANC131, 8ANC134, B12, B13, F105, JM4, NIH45-46, PGT128, PGT135, PGT151, VRC-PG04, VRC01, VRC07, VRC13, VRC16, VRC18, VRC23, VRC27.

For a particular residue *i*, the average biochemical similarity, $\bar{s}_i$, between the observed non-consensus amino acids and the respective consensus amino acid for that residue was obtained using the following formula:

$$\bar{s}_i = \frac{\sum_{j=1}^{n_{panel}} s_i(x_{ji}, c_i)[1-\delta(x_{ji}, c_i)]}{\sum_{j=1}^{n_{panel}} [1-\delta(x_{ji}, c_i)]} \qquad \text{(S25)}$$

where n_{panel} is the number of sequences in the CATNAP panel, x_{ji} is the amino acid at residue *i* of the j-th panel sequence, c_i is the consensus amino acid at residue *i*, $s_i(a, b)$ is the similarity between amino acids *a* and *b*, as defined in (17), and δ is the Kronecker delta function which is unity if the two arguments are equal. This quantity reflects the average similarity between consensus and non-consensus amino acids within the CATNAP panel.

Supplementary Figures and Tables

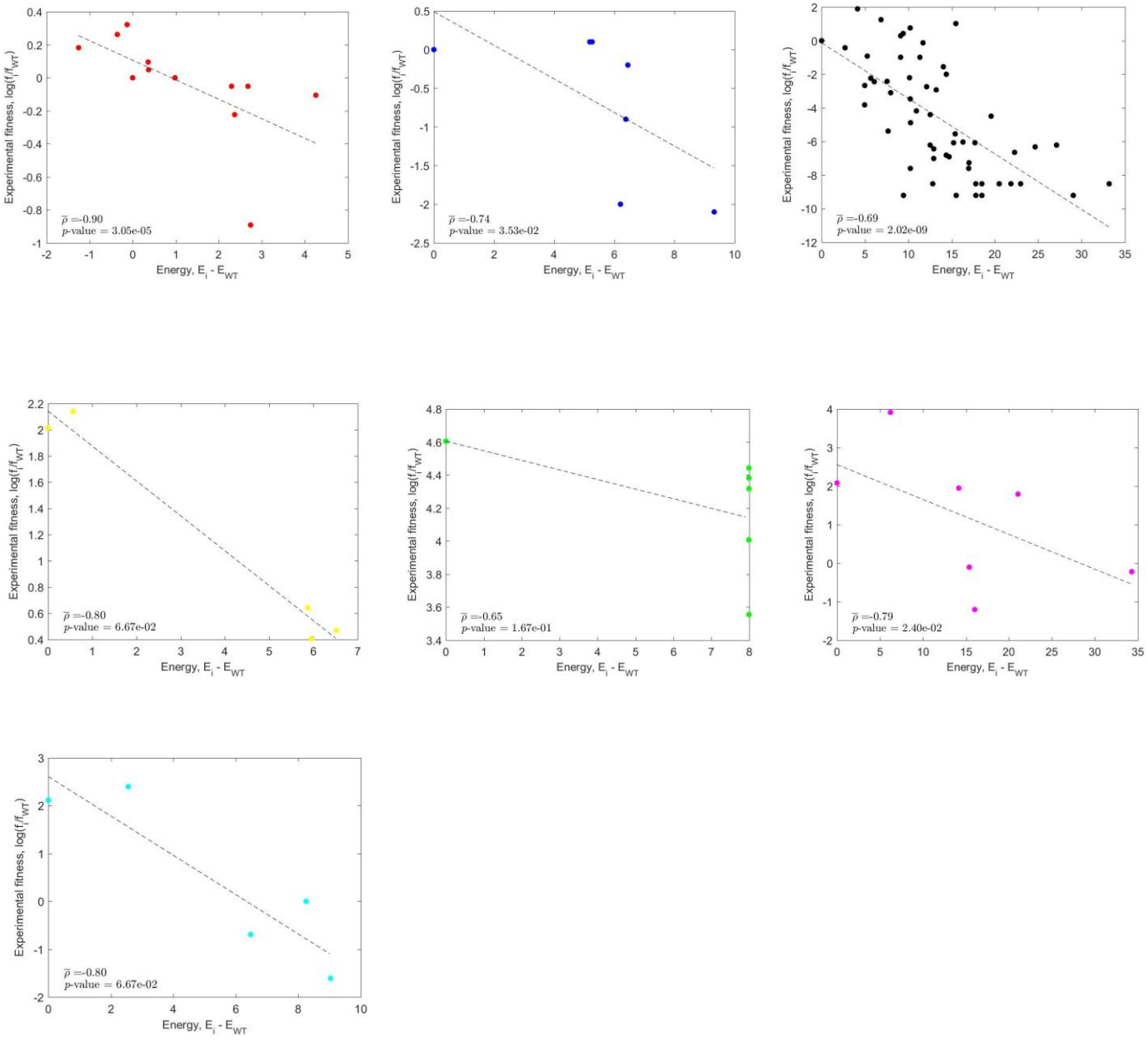

Fig. S1. Logarithm of fitness vs. energy normalized by the reference strain for the seven experiments collected from literature using a combining factor $\phi = 0.95$, for gp160. A strong negative correlation is observed for all experiments. The experimental values are taken clockwise respectively from (18), (19), (20), (21), (22), (23) and (21).

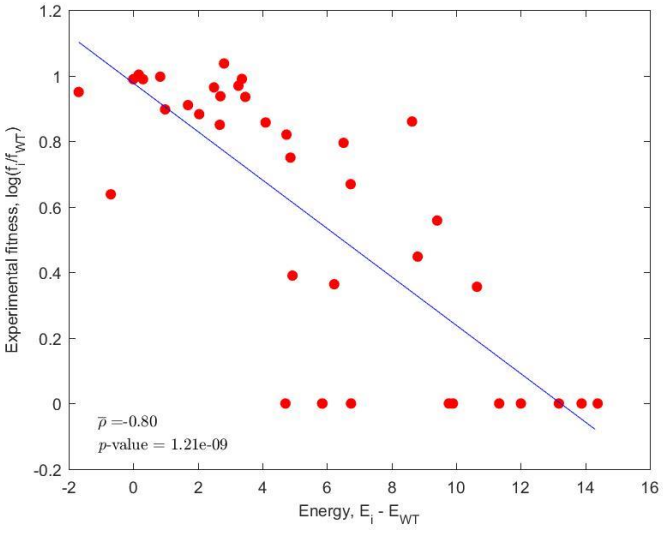

Fig. S2. Logarithm of fitness vs. energy normalized by the reference strain for p24. A strong negative correlation is observed.

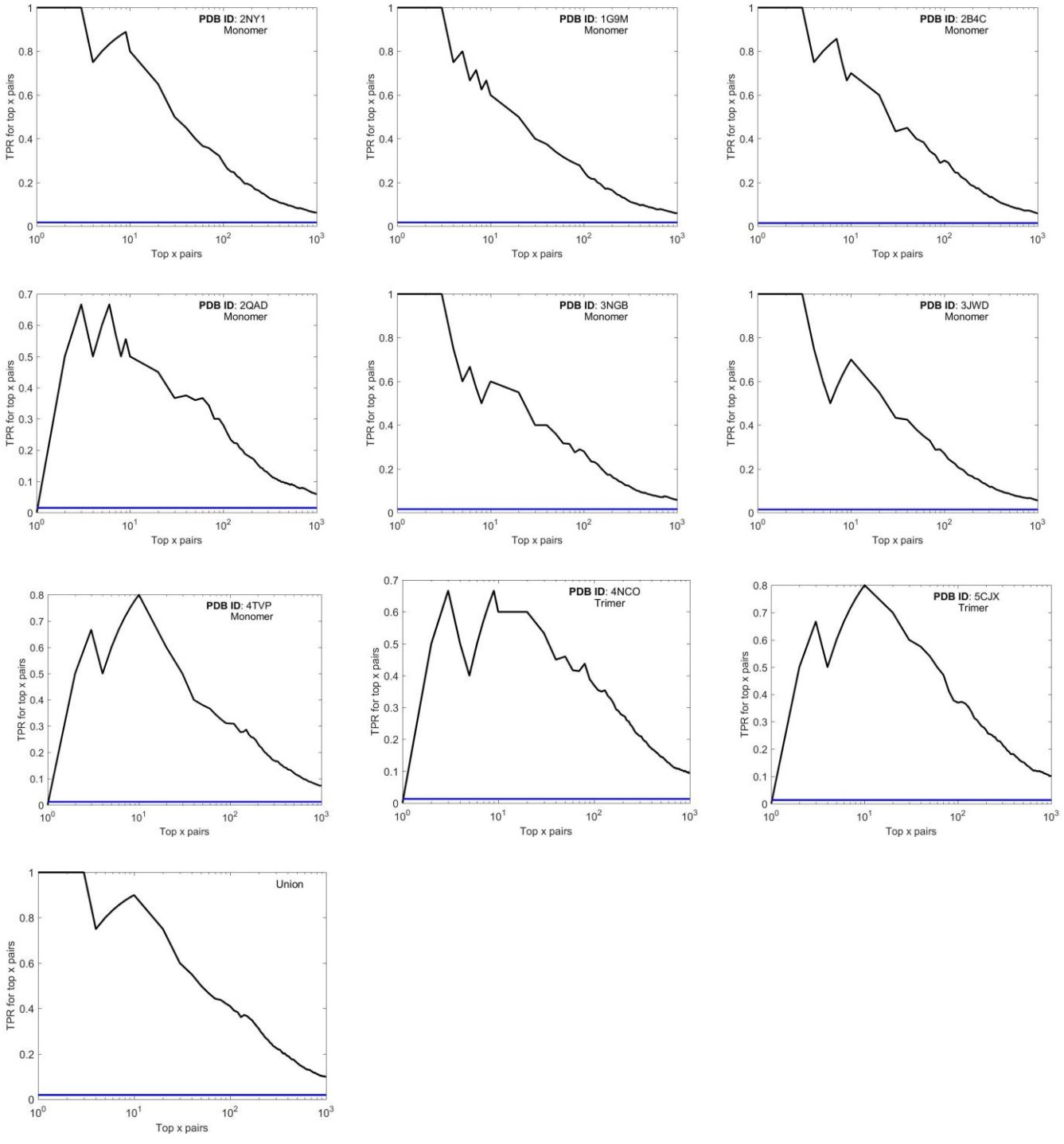

Fig. S3. Fraction of contacts in the top *x* predicted pairs which are actually in contact (true positive rate (TPR)) vs the top *x* pairs (black line). Also plotted is the total number of contacts divided by the total number of pairs (horizontal blue line), which represents the probability of choosing a pair in contact purely by chance. Only pairs > 5 distance apart in sequence space are considered, and out of these pairs, two residues are assumed to be in contact if they are < 8Å apart. The last figure shows the TPR curve using the union of all contact maps.

Method	Weighted Correlation of Fitness vs Energy (fitness rank ordering prediction)
MPF-BML	-0.7353
MPF	-0.6918
Fields only	-0.6870
mfDCA	-0.4378

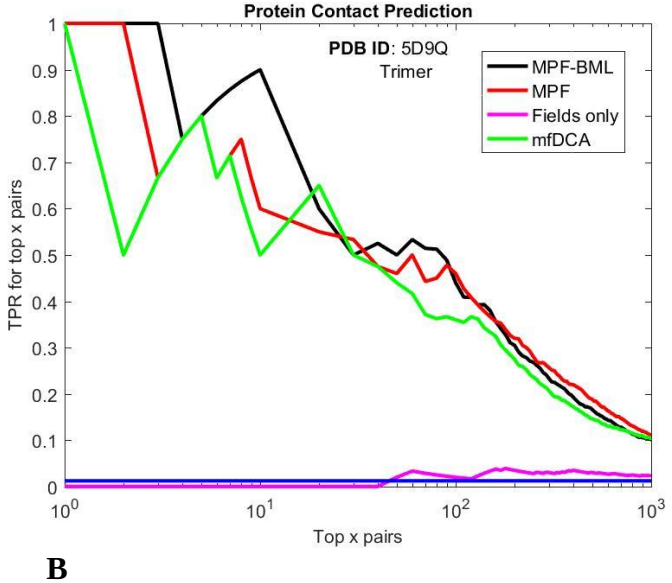

A **B**

Fig. S4. A) Average weighted correlation between experimental fitness and predicted energy. B) Fraction of contacts in the top *x* predicted pairs which are actually in contact (true positive rate (TPR)) vs the top *x* pairs (black line). Predictions are made by four different models: MPF/BML (the model using our framework), MPF (the model using our framework without BML), a fields only model (fields are matched only to the single mutant probabilities and couplings are zero), and mfDCA (mean-field approach) (13).

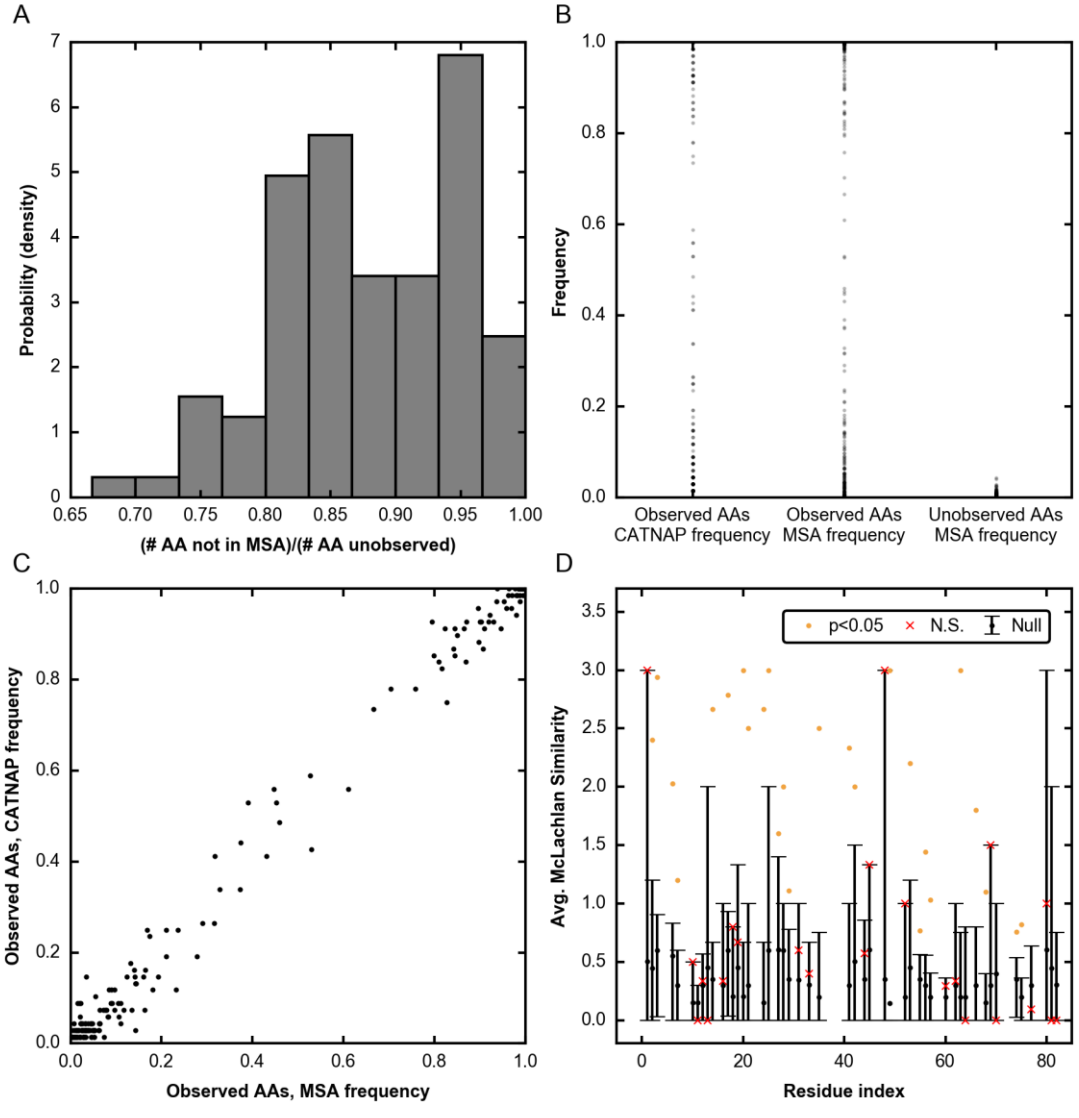

Fig. S5. Further analysis of CATNAP data. A) Histogram, over the residues in the CD4bs bnAb footprints, of the fraction of amino acid (AA) mutations that are not observed in the MSA used to fit the landscape, out of all mutations not observed in the CATNAP data. B) Frequencies of amino acid mutations classified in three ways: 1. "Observed AAs, CATNAP frequency" consists of the CATNAP frequencies of mutations observed in CATNAP; 2. "Observed AAs, MSA frequency" consists of the MSA frequencies of mutations observed in CATNAP; and 3. "Unobserved AAs, MSA frequency" consists of the MSA frequencies of mutations unobserved in CATNAP. C) Comparison of MSA and CATNAP frequencies for amino acid mutations observed in CATNAP. D) Average McLachlan similarity between consensus and non-consensus amino acids at non-IC-50 observed in the CATNAP panels for the bnAbs studied. The values are compared with a null distribution in which the non-consensus amino acids found in the CATNAP viruses are replaced with random amino acids chosen uniformly from all possible non-consensus amino acids. The error bars plotted are from the minimum to the 95th percentile. For residues having average similarity in the top 95th percentile of null model, this average is plotted as an orange dot, while the remaining (not significant) are plotted as red crosses. Missing data indicates a residue that had no non-consensus amino acids represented in the CATNAP data.

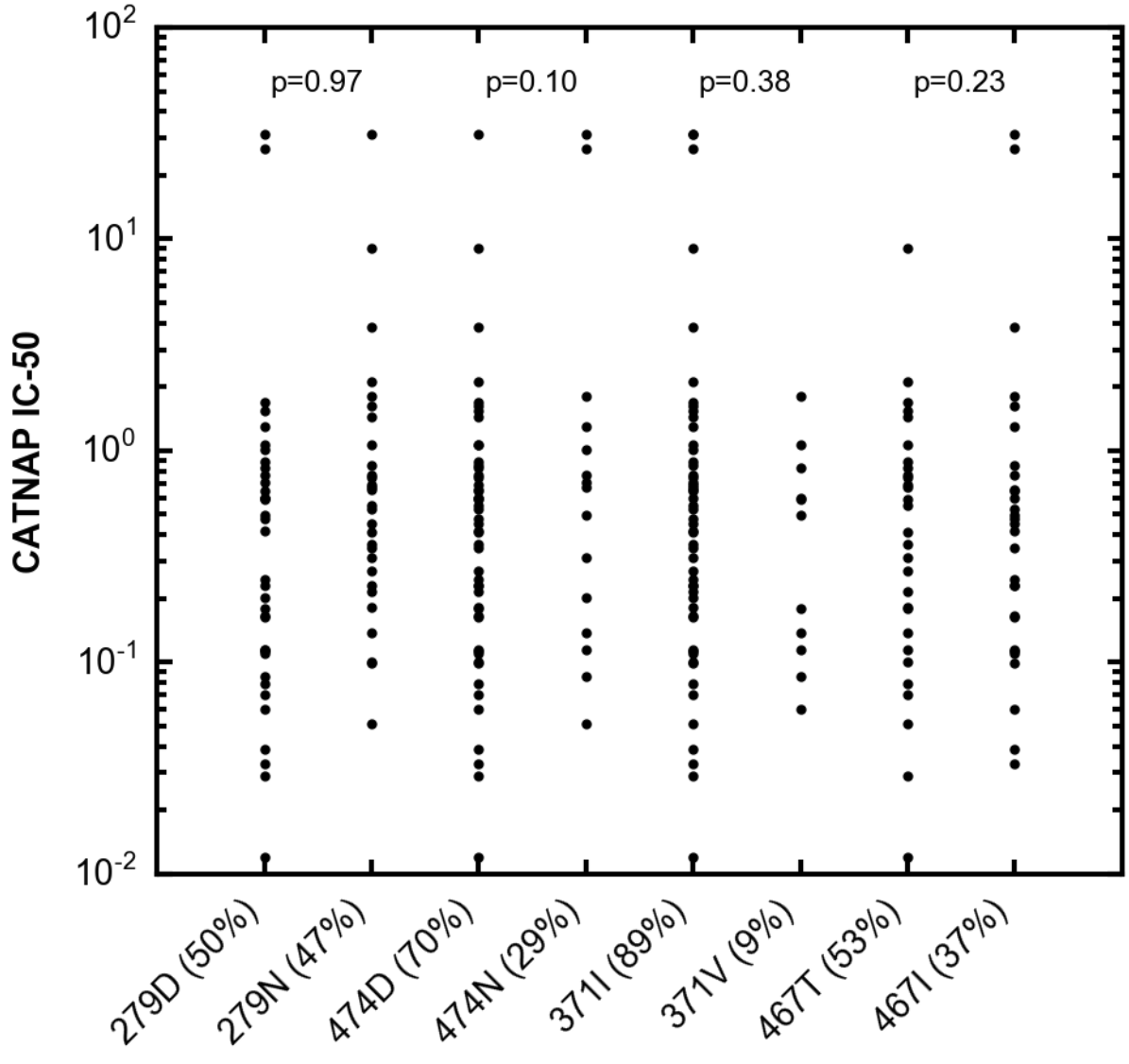

Fig S6. IC-50 values in the CATNAP panel for bnAb VRC01, for four residues (279, 474, 371, 467) which have low predicted fitness cost. The IC-50 values are split into two groups based on whether the sequence has the consensus or most common mutant amino acid, labeled on the x-axis; e.g. 279D (50%) indicates sequences in the panel in which residue 279 has amino acid D, which is present in 50% of sequences in the MSA used to fit our landscape. P-values are shown for each residue, and indicate that the distribution of IC-50 values for sequences containing either consensus or most common mutant amino acid at a particular residue are statistically indistinguishable using a two-tailed t-test.

Protein	**No. param**	**Avg. ent.**	**Length, *L***	**Avg. no. mut.**
gp160	28,262,831	0.46	856	7.78
RT	3,153,651	0.12	440	4.71
p24	1,143,462	0.09	231	5.55
Integrase	1,141,235	0.12	288	4.25
p17	729,218	0.26	132	8.18
nef	569,292	0.36	205	5.50
vif	519,117	0.30	192	5.30
protease	323,981	0.33	99	7.17
p15	238,351	0.14	120	4.77
rev	198,462	0.39	116	6.25
p6	155,691	0.33	52	9.82
p7	132,960	0.22	55	8.45
vpu	99,951	0.45	82	7.29
p2	10,358	0.49	14	9.64
p1	9,914	0.13	16	8.06

Table S1. Number of parameters, average entropy (over all residues), length and average number of mutants (over all residues) using the HXB2 sequence as a reference sequence, and based on the amino acid multiple sequence alignment (MSA) of HIV-1 Clade B gp160 sequences from the Los Alamos National Laboratory HIV sequence database (www.hiv.lanl.gov; accessed 11th Dec, 2016). gp160 has the largest number of parameters (without combining mutants) and approximately 9× more parameters than the protein (RT) with the second largest number. As gp160 has the second largest entropy, it also has the largest number of parameters after appropriate combining of mutants (e.g. using (S13)).

ϕ	**Mean of** $\beta_i(\phi)$	**Number of parameters**
0	78.8285	332,520
0.1	78.8285	332,520
0.2	77.87298	334,150
0.3	75.52216	337,420
0.4	66.94252	353,190
0.5	54.21058	384,050
0.6	41.60982	441,170
0.7	24.29135	593,120
0.8	10.77352	965,830
0.9	3.010148	2,394,300
0.95	0.816736	4,415,500
1	0	26,070,000

Table S2. The mean of $\beta_i(\phi)$ for different ϕ, and the corresponding number of parameters. We observe that the mean is close to one when $\phi = 0.95$.

Exp. *i*	**Ref.**	N_i	$\phi = 0$	$\phi = 0.2$	$\phi = 0.4$	$\phi = 0.6$	$\phi = 0.8$	$\phi = 0.95$	$\phi = 1$
1	(18)	12	-0.57	-0.59	-0.74	-0.79	-0.84	-0.90	-0.85
2	(19)	7	-0.20	-0.20	-0.31	-0.27	-0.40	-0.74	-0.70
3	(20)	56	-0.60	-0.62	-0.59	-0.61	-0.67	-0.69	-0.63
4	(21)	5	-0.56	-0.87	-0.87	-0.56	-1.00	-0.80	-0.80
5	(22)	6	-0.65	-0.65	-0.65	-0.65	-0.65	-0.65	-0.85
6	(23)	7	-0.71	-0.71	-0.75	-0.71	-0.71	-0.79	-0.43
7	(21)	5	-0.67	-0.67	-0.67	-0.67	-0.80	-0.80	-0.80
		$\bar{\rho} =$	-0.58	-0.61	-0.62	-0.62	-0.70	-0.74	-0.68

Table S3. For different combining factors ϕ, and for seven different experiments, the Spearman correlation between measured fitness and the energy as calculated from the prevalence landscape is shown (fourth to tenth column). The parameter N_i denotes the number of fitness measurements for the *i*th experiment. The last row shows the weighted Spearman correlation (Eq. S19). This correlation is strongest when $\phi = 0.95$ (for which, there is a strong correlation for each individual experiment), providing validation for the data-driven choice of the combining factor ϕ.

Residue i	Residue j	Distance (Å)	Function
389	417	9.3763	Both in V4 Loop
65	208	9.0257	?
192	426	21.6352	192 in V2 Loop, 426 is a CD4 contact
178	195	14.2069	Both in V2 Loop
279	474	15.1180	Both are CD4 contacts
164	195	9.5545	Both in V2 Loop
178	194	9.3138	Both in V2 Loop
170	178	24.2928	Both in V2 Loop

Table S4. The eight residue-pairs predicted by our landscape to be in contact, but are not in contact according to PDB structure 5D9Q. The distance between residues and functional domains are indicated. We observe that with the exception of one residue-pair, all pairs are either in the V2 or V4 loop, or are CD4 contacts.

Residue type	HXB2 #	Neutralization CD4-Ig (%)	Binding VRC01 (%)	Escape cost
High fitness **cost, low affinity**	**368**	ND	3	7.35
	367	ND	28	6.84
	457	ND	29	6.57
High fitness **cost, moderate affinity**	**473**	ND	79	6.90
	458	ND	84	6.69
	366	ND	50	6.44
	469	ND	62	6.44
	427	ND	76	6.02
	280	ND	66	5.68
Other	**456**	55	80	6.10
	276	29	193	5.61
	430	>10000	98	5.15
	459	722	63	4.95
	282	5	68	4.68
	97	184	88	4.67
	455	22	65	4.37
	365	32	149	4.18
	283	5	78	3.04
	476	5	55	2.86
Low fitness cost, low affinity	**371**	ND	30	3.12
	474	11	20	2.79
	279	2	0	2.13
	467	ND	28	1.99

Table S5. VRC01 bnAb contact residues (as determined by (24)), characterized by experimental loss of neutralization sensitivity to CD4-Ig and loss of binding affinity for respective Alanine scanning mutants, reported as percent neutralization sensitivity or binding affinity of mutant compared to wild type. ND indicates that the Alanine mutant did not support entry. The "high fitness cost, low affinity" residues greatly diminish VRC01 binding affinity (<33%) when mutated to Alanine, and are predicted to have high fitness cost. The "high fitness cost, moderate affinity" residues are less detrimental to affinity, but do not support entry, which is reflected in our high predicted fitness costs. The "low fitness cost, low affinity" residues result in diminished VRC01 affinity upon mutation to Alanine, but are paradoxically predicted to have low fitness cost despite their low sensitivity to neutralization by CD4-Ig. This is explained in the main text by the high prevalence of the most-common mutant amino acid for each of these residues.

References

1. Shekhar K, et al. (2013) Spin models inferred from patient-derived viral sequence data faithfully describe HIV fitness landscapes. *Phys Rev E - Stat Nonlinear, Soft Matter Phys* 88:1–10.
2. Jensen MA, et al. (2003) Improved coreceptor usage prediction and genotypic monitoring of R5-to-X4 transition by motif analysis of human immunodeficiency virus type 1 env V3 loop sequences. *J Virol* 77(24):13376–88.
3. Ferguson AL, et al. (2013) Translating HIV sequences into quantitative fitness landscapes predicts viral vulnerabilities for rational immunogen design. *Immunity* 38(3):606–617.
4. Barton JP, Leonardis E De, Coucke A, Cocco S (2016) ACE: Adaptive cluster expansion for maximum entropy graphical model inference. *Bioinformatics* 32(20):3089–3097.
5. Sohl-Dickstein J, Battaglino P, DeWeese MR (2011) Minimum Probability Flow learning. *Proceedings of the 28th International Conference on Machine Learning*, pp 905–912.
6. Riedmiller M, Braun H (1993) A direct adaptive method for faster backpropagation learning: The RPROP algorithm. *IEEE International Conference on Neural Networks*, pp 586–591.
7. Barton JP, et al. (2016) Relative rate and location of intra-host HIV evolution to evade cellular immunity are predictable. *Nat Commun* 7(5):1–10.
8. Barton J, Cocco S (2013) Ising models for neural activity inferred via selective cluster expansion: structural and coding properties. *J Stat Mech Theory Exp* (3):1–57.
9. Field A (2001) Meta-analysis of correlation coefficients: A Monte Carlo comparison of fixed- and random-effects methods. *Psychol Methods* 6(2):161–180.
10. Mann JK, et al. (2014) The fitness landscape of HIV-1 gag: Advanced modeling approaches and validation of model predictions by in vitro testing. *PLoS Comput Biol* 10(8):1–11.
11. Weigt M, White RA, Szurmant H, Hoch JA, Hwa T (2009) Identification of direct residue contacts in protein-protein interaction by message passing. *Proc Natl Acad Sci* 106(1):67–72.
12. Dunn SD, Wahl LM, Gloor GB (2008) Mutual information without the influence of phylogeny or entropy dramatically improves residue contact prediction. *Bioinformatics* 24(3):333–340.
13. Morcos F, et al. (2011) Direct-coupling analysis of residue coevolution captures native contacts across many protein families. *Proc Natl Acad Sci* 108(49):E1293-301.
14. Sneath PHA (1966) Relations between chemical structure and biological activity in peptides. *J Theor Biol* 12(2):157–195.
15. Jardine JG, et al. (2016) Minimally mutated HIV-1 broadly neutralizing antibodies to guide reductionist vaccine design. *PLoS Pathog* 12(8):1–33.
16. Fisher R (1922) On the interpretation of $\chi 2$ from contingency tables, and the calculation of P. *J R Stat Soc* 85(1):87–94.
17. McLachlan AD (1972) Repeating sequences and gene duplication in proteins. *J Mol Biol* 64(2):417–437.
18. Troyer RM, et al. (2009) Variable fitness impact of HIV-1 escape mutations to cytotoxic T lymphocyte (CTL) response. *PLoS Pathog* 5(4):30–34.
19. Liu Y, et al. (2014) A sensitive real-time PCR based assay to estimate the impact of amino acid substitutions on the competitive replication fitness of human immunodeficiency virus type 1 in cell culture. *J Virol Methods* 189(1):157–166.
20. da Silva J, Coetzer M, Nedellec R, Pastore C, Mosier DE (2010) Fitness epistasis and constraints on adaptation in a human immunodeficiency virus type 1 protein region. *Genetics* 185(1):293–303.
21. Lobritz MA, Marozsan AJ, Troyer RM, Arts EJ (2007) Natural variation in the V3 crown of human immunodeficiency virus type 1 affects replicative fitness and entry inhibitor sensitivity. *J Virol* 81(15):8258–69.
22. Kassa A, et al. (2009) Identification of a human immunodeficiency virus type 1 envelope glycoprotein variant

resistant to cold inactivation. *J Virol* 83(9):4476–88.

23. Anastassopoulou CG, et al. (2007) Escape of HIV-1 from a small molecule CCR5 inhibitor is not associated with a fitness loss. *PLoS Pathog* 3(6):720–732.

24. Li Y, et al. (2011) Mechanism of neutralization by the broadly neutralizing HIV-1 monoclonal antibody VRC01. *J Virol* 85(17):8954–8967.